Separating the roles of magnetic topology and neutral trapping in modifying the detachment threshold for TCV

A. Fil*,[1] B. Lipschultz,[1] D. Moulton,[2] B. D. Dudson,[1] O. Février,[3] O. Myatra,[1] C. Theiler,[3] K. Verhaegh,[1,3] M. Wensing,[3] EUROfusion MST1 teams,[4] and the TCV team[5]

[1] *York Plasma Institute, University of York, Heslington, York, YO10 5DQ, UK*
[2] *Culham Centre for Fusion Energy, Culham Science Centre, Abingdon, OX14 3DB, UK*
[3] *Ecole Polytechnique Fédérale de Lausanne (EPFL), Swiss Plasma Center (SPC), CH-1015 Lausanne, Switzerland*
[4] *See author list of "B. Labit et al 2019 Nucl. Fusion 59 086020 (https://doi.org/10.1088/1741-4326/ab2211)"*
[5] *See author list of "S. Coda et al 2019 Nucl. Fusion 59 112023"*

Correspondence: *Alexandre Fil. Email: alexandre.fil@ukaea.uk

Keywords: Tokamak, TCV, SOL, Detachment, SOLPS-ITER

Abstract.

Total flux expansion, a divertor magnetic topology design choice embodied in the Super-X divertor, is predicted through simple analytic models and SOLPS calculations to reduce the plasma and impurity density detachment thresholds as the outer divertor separatrix leg position and the strike-point major radius, R_t, are increased. However, those predictions are contradicted by recent TCV experimental results. In this study, utilizing the SOLPS-ITER code, we are able to both match TCV results and demonstrate that the effect of total flux expansion is counteracted by two other divertor geometry design characteristics that affect neutrals: a) the strike-point angle to the outer target; and b) the effect of physical baffles that reduce the amount of neutrals escaping from the divertor. We quantify the role of those neutral effects through developing and applying a quantitative definition of neutral trapping. The results of this study indicate that improved divertor design, properly utilizing the three design characteristics discussed should lead all effects to be additive in reducing the detachment threshold. A second implication of this study is that any assessment of alternative topologies must separate out the effects of magnetic topology from neutral design characteristics.

1 Introduction

It is generally thought that the process of divertor detachment is required to reduce the power to the divertor targets of a fusion reactor, to below engineering limits. A series of papers have even argued that without raising total plasma radiation fractions to values of over 95%, the reactor power flow towards the divertor will be too high for detachment to overcome [1][2]. A number of 'alternative' divertor magnetic topologies are being studied, through experiment [3][4][5][6][7], simple analytic models [4][8][9] and numerical models [10][11]. All of them include variations in divertor magnetic geometry compared to the 'conventional' divertors of the last 30 years, which have focused on 'vertical-target' and 'horizontal-target' designs [12][13][14][15][16][17]. An important goal of current divertor studies is thus to quantify whether the divertor 'performance' is improved or degraded by any new magnetic topology compared to conventional divertors.
The differences in divertor magnetic geometry embodied by the alternative divertors can be described by the following attributes:

a) Poloidal flux expansion, which adds field line length in the divertor, achieved by the addition of a second x-point which can be located near the primary one that forms the divertor (snowflake [18]), near the target (X-point target [19]) or just outside the vessel (X-divertor [20]).

b) Total flux expansion [8][10], achieved by lowering the total field at the strike-point (where the separatrix intersects the target), $|B_{tot,target}|$ compared to that upstream ('u') at the x-point or midplane, by shifting the target to larger major radius (R_t) as in a Super-X divertor [21]. Total flux expansion is quantified as $|B_{tot,u}|/|B_{tot,target}|$. Under the assumption that the total field is dominated by the toroidal field, total flux expansion has also been approximated by $f_R \sim R_t/R_u$ [4].

c) Increasing the number of divertor separatricies/legs to spread the power (snowflake).

d) Having two x-points close together (snowflake) creates an extended low poloidal field region which is predicted [22] and measured [23] to encourage cross-field transport.

e) Some combination of the above as, for example, the 'quasi-snowflake' [24] where the second x-point is close to the primary one (as in a snowflake), but also close to the target like an X-divertor.

One general characteristic of poloidal flux expansion is to increase the field line length in the divertor, which would encourage cross-field transport through diffusion and possibly encourage turbulent transport as well [25]. On the other hand, total flux expansion increases the cross-sectional area of a flux tube, which

lowers the parallel heat flux, $q_{t,\parallel} \propto |B_{tot,target}|$. In most cases $|B_{tot}|$ is dominated by the toroidal field and so $q_{t,\parallel} \propto \frac{1}{R_t}$ [4][8]. The difficulty in properly evaluating any of the above new divertor magnetic topologies is that one must separate out any new topology-derived effect from other characteristics of existing divertors. For example, the poloidal angle between the separatrix and the target (or 'strike-point angle') affects the detachment threshold. An angle less than 90 degrees (more typically 15-30), historically termed 'vertical-target' [15][26], sends recycled neutrals back towards the separatrix and into the private flux region. This leads to more neutrals near the separatrix to be ionized and to raise (lower) the plasma density (temperature) [12][15][27]. The opposite strike-point angle ($>$ 90 degrees), termed 'horizontal-target', sends more recycled/reflected neutrals towards the common flux region, leading to less ionization in the near separatrix region. The lower T_e, and higher n_e of the vertical target encourages more power losses and, as was shown for the initial implementation of the vertical target divertor [15][26], leads to a lower detachment threshold than for a horizontal target. Modelling has demonstrated this effect for JET [27].

We must also take into account how 'closed' the divertor is to neutrals trying to escape to the midplane. A closed divertor can be expected to increase (decrease) the plasma density (temperature) in the divertor compared to neutrals easily escaping the divertor, no matter what the strike-point angle is since the neutral density is increased throughout the entire divertor. Since some level of mechanical baffling typically accompanies the vertical target, the relative effect of baffling vs strike-point angle is not easily separated even for current divertors - and has not been to our knowledge.

One goal of the present study is to compare a 'Super-X' divertor topology (higher-R_t, higher total flux expansion), to a 'conventional' divertor topology (lower-R_t. lower total flux expansion) on TCV. The effect of total flux expansion on target temperatures and densities has already been investigated [4], relying on the 2-point model. It was shown that the target electron density and temperature scale approximately with f_R^2 $[(\frac{B_u}{B_t})^2]$ and $1/f_R^2$ $[(\frac{B_t}{B_u})^2]$, respectively, while keeping other quantities such as P_{SOL} and the radiation loss, f_{loss}, constant. Assuming that the target temperature at detachment remains constant, this translates into the upstream density detachment threshold decreasing as $1/f_R$ $[(\frac{B_t}{B_u})]$.

A second simple 'thermal front' model [8] predicts both the detachment threshold and the location of the detachment front between the target and x-point as detachment proceeds. It includes energy balance as in the 2-point model as well as a self-consistent inclusion of impurity radiation due to an impurity concentration, C_Z, which is constant along the field line modelled. It leads to the same prediction of the scaling of upstream density detachment threshold, $n_{u,detach} \sim B_t/B_u$ but also makes predictions for the detachment threshold

in $C_Z[\sim (B_t/B_u)^2]$ and $P_{SOL}[\sim (B_t/B_u)^{-7/5}]$ (where B_u is specified as the magnetic field amplitude at the X-point [8]). Any confirmation of the total flux expansion scaling for the detachment threshold in upstream density would thus support predictions for thresholds in P_{SOL} and C_Z.

2D SOLPS simulations, which include much more physics than the analytic models, have confirmed the analytic predictions by showing that $T_{e,t}$ and $n_{e,t}$ (target electron temperature and density) scale with $1/f_R^2$ $[(\frac{B_t}{B_u})^2]$ and f_R^2 $[(\frac{B_u}{B_t})^2]$, respectively, and also confirmed the upstream density detachment threshold dependence on $1/f_R$ $[(\frac{B_t}{B_u})]$. That SOLPS-based study utilized a "box" divertor geometry [10] which was designed to allow only changes in total flux expansion (magnetic topology), as opposed to divertor geometry and recycling, by rotating the box around the X-point and thus increasing the radial position of the outer strike-point. Additional SOLPS simulations, utilizing the more closed (to neutrals) geometry of MAST-U [28], have also demonstrated the beneficial effect of total flux expansion [29] by comparing different MAST-U magnetic equilibria from 'conventional' (large $\frac{B_t}{B_u}$) to 'Super-X' (smaller $\frac{B_t}{B_u}$), consistent with the models and modelling cited above. The Super-X was also found to require much lower C_Z to detach than the conventional topology for the same upstream conditions as described above [29].

In contrast to the SOLPS and analytic results, UEDGE modeling [11] with fluid neutrals, found that the divertor leg length had a stronger effect on the P_{SOL} detachment threshold than total flux expansion (over the range that those parameters were changed in that study). A significant difference to the modeling reviewed above were the use of fluid neutrals and that the divertor chamber/channel very closely fit to the outer divertor leg along its entire length which should strongly trap neutrals in the divertor leg region.

Experimental results from TCV and DIII-D are also mixed in terms of the effect of total flux expansion. In DIII-D experiments using the lower, open, horizontal target divertor [4], the outer strike-point major radius was scanned across the entire bottom of the tokamak (1.2 to 1.6 m) and the strike-point density and temperature monitored. The study identified two sub-regions: the region from the inner wall to the pump opening ($R_t = 1.2 - 1.37$ m, the pump was not turned on) - designated the 'floor' region, and the region from just past the pump opening outward ($R_t = 1.37 - 1.6$ m) - designated the 'shelf' region. Within each of those regions, and with conditions being either L- or H-mode, the scaling of target density and temperature was either as predicted by total flux expansion ('shelf') or had a dependence on R_t that was even stronger than the analytic predictions of total flux expansion ('floor'). When moving between the two regions, the scaling of $n_{e,t}$ and $T_{e,t}$ was weaker than the analytic predictions. The study, which also included SOLPS modeling, attributed the difference in the R_t scaling between the floor and the shelf to differences in neutral trapping/recycling, being

better in the floor region (the floor traps neutrals better than the shelf due to the proximity of the strike-point to the pump opening, where neutrals were trapped and built up without the pump turned on). That modeling (and the paper itself) did not directly address the effect of total flux expansion on detachment thresholds. The results of recent TCV experiments [3] contrast strongly with the DIII-D R_t studies described above. The variation of the outer divertor strike-point across the entire open, horizontal target region at the bottom of the machine revealed a lack of total flux expansion effect on the detachment density threshold or on the target temperature and density. If anything, the target density decreased as R_t was increased and the density detachment threshold slightly increased.

The goal of this paper is to understand and explain the lack of total flux expansion effect in those TCV plasmas using the 2D transport code SOLPS-ITER [30] [31]. The modeling recovers the TCV experimental results while generally matching experimental conditions. Additional extensive modeling demonstrates that the effect on the detachment threshold of each of the two neutral effects listed above are enhanced for low-R_t compared to high-R_t in such a way as to negate the effect of total flux expansion: a) the strike-point target angle/geometry changes from vertical to horizontal-target in moving from low to high-R_t; and b) the effective trapping of neutrals in the divertor is reduced as R_t is increased.

These neutral effects are made more equal in their effect on low- and high-R_t divertor plasmas through changes in the SOLPS-ITER divertor geometry, resulting in the R_t effect being recovered. We do this by enforcing the same strike-point angle for the two R_t cases and by also "closing" the divertor with baffling, reducing the escape of neutrals to the midplane.

In the process of varying the neutral characteristics of the TCV divertor, we have also been able to quantify the separate effects of neutral baffling closure and strike-point angle. That quantification is accomplished by using a new definition of the neutral trapping based on the fraction of integrated ion flux to the target that is ionized in a near-separatrix bundle of flux tubes, chosen as the numerically-resolved flux tubes where the target heat flux peaks during the attached phase.

In the following section, we review the TCV experimental results and their characteristics as well as its modelling with SOLPS-ITER. This is followed by section 3 where the definition of neutral trapping (for which we use the symbol η_{RI}) is made and the various neutral and total flux expansion effects compared for their effect on the upstream density detachment threshold and η_{RI}. We will then discuss the results and their consequences in section 4 before concluding in section 5.

2 Total flux expansion effect on TCV detachment

2.1 Experimental total flux expansion scan in TCV

Experiments on the TCV tokamak [3] [32] were recently conducted to investigate the effect of total flux expansion on detachment, especially its effect on the detachment density threshold. During these experiments, the midplane separatrix density was linearly increased in time for 4 different outer divertor strike-point major radii, R_t, ranging from 0.62 m to 1.06 m, a change in total flux expansion of ~ 1.74. The shape of the separatrix around the core of the plasma was held roughly constant for all 4 cases. Special care was taken to obtain similar upstream plasma conditions (including density, parallel connection length, input power and power crossing the separatrix).

We focus on the two best-diagnosed TCV configurations in this paper, which are shown on Figure 1. Both are Ohmic L-mode plasmas with a plasma current, I_p, of 320 kA, and a toroidal field on the core axis, B_T, of 1.42 T. In those pulses, the upstream separatrix density was ramped up from 0.35 n_G to 0.75 n_G (where n_G is the Greenwald density). The two configurations correspond to R_t of ~ 0.68 m (TCV pulse 52066, referred to as the "low-R_t" divertor configuration) and ~ 0.92 m (52064, referred to as the "high-R_t" configuration). The corresponding total flux expansion change is ~ 1.3 (Ratio of the magnetic fields at the strike-point between the two configurations; not exactly equal to the inverse ratio of the two major radii, which gives 1.35 instead of 1.3, due to the poloidal field).

The behavior of the peak (and total) ion current to the outer target is one of the main measurements used to determine when and if detachment occurs: As the upstream density is increased, the target current increases during the attached phase (pre-detachment) and then, during the detached phase, decreases ("roll-over"). That behavior is shown in Figure 2 as determined by Langmuir probe [34] measurements of the target ion current. The probe location monitored is that which is closest to the radial peak of the heat flux profile before roll-over. We then follow the measurements made utilizing that probe for the whole shot. For those two shots, the chosen probe almost always corresponds to the peak ion flux, as plotted in [3]. We note that volumetric momentum losses, associated with detachment onset, can start before the roll-over of the flux-tube or the full target ion current [35]. However, volumetric momentum measurements are much harder to make and make accurately. Thus, we have relied on the roll-over of the peak target ion current in time as a measure of the detachment threshold. The density detachment thresholds for the two experimental R_t cases are not very different and it seems that the low-R_t case (52066) rolls-over at lower upstream density than the high-R_t case (52064), according to measurements of the total ion current (not shown), peak ion current and the

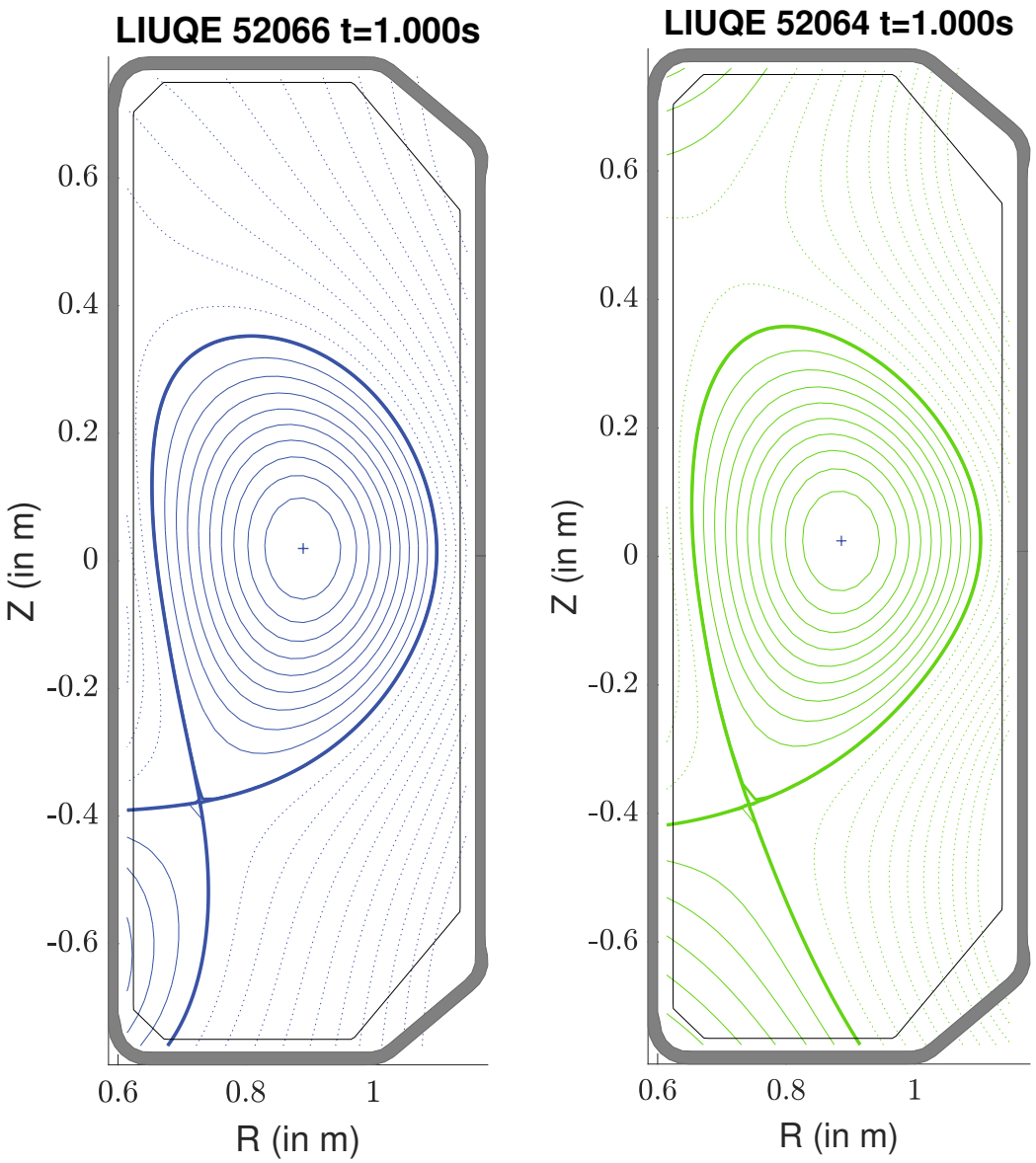

Figure 1: Equilibrium of two TCV shots with different total flux expansion: 52066 at 1 second (low-R_t) and 52064 at 1 second (high-R_t). Equilibrium reconstruction done with LIUQE [33]. The outer divertor R_t for the low- and high-R_t cases shown are 0.68 and 0.92 m. The factor increase in total flux expansion from high- to low-R_t is ~ 1.3.

CIII emissivity front movement, as reported previously in [3]. Recent experiments with TCV H-mode plasmas appear to be consistent with the L-mode results shown herein [36]. The experimentally-determined TCV ratio of upstream detachment thresholds between the two different configurations, or N_{thres} (see equation 1), is difficult to estimate due to uncertainties of the measurement of the experimental upstream density. Figure 2 and the CIII front movement [3] give an N_{thres} of ~ 0.85 but this value is rather uncertain due to the

uncertainty of the separatrix position.

$$N_{thres} = (n_{eu,rollover})_{low-R_t}/(n_{eu,rollover})_{high-R_t} \quad (1)$$

The experimental results are in contrast to what we would expect from simple predictions of just the total flux expansion effect - that the low-R_t case should have a higher density detachment threshold by a factor $N_{thres} = 1.3$.

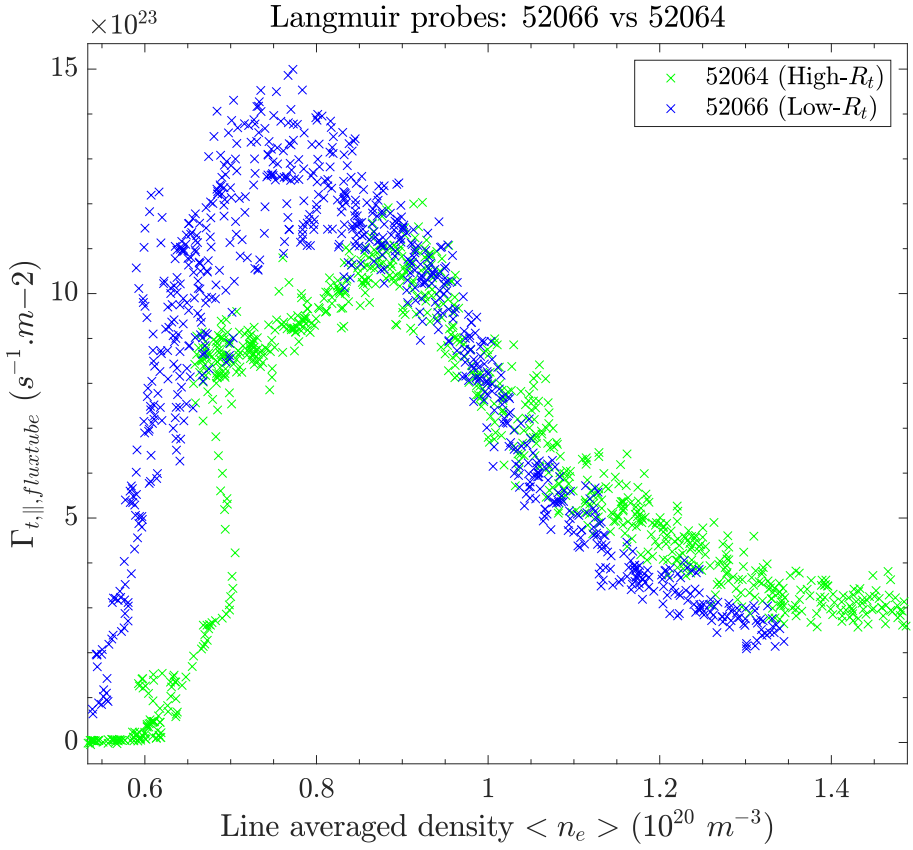

Figure 2: Evolution of the parallel ion flux to the outer target for the probe where the target heat flux is peaked in attached conditions. The two corresponding equilibria are shown in Figure 1.

Even prior to detachment, the TCV results contradict the prediction of the theoretical models [4][8] and the modeling work [10] described in the introduction. Measurements of the target electron density for the same upstream density during the attached phase for both low-R_t and high-R_t configurations are approximately

the same within experimental uncertainties for the same upstream conditions. That is in contrast to the predicted ratio for the high- to low-R_t target densities of 1.3^2. This suggests the presence of additional effects (as concluded in [3]). In the following, we model those two TCV experimental shots with SOLPS-ITER in order to obtain a better understanding of the experimental observations. Our conclusion is that differences in divertor geometry between the low- and high-R_t cases (strike-point angle and neutral trapping) compensate for the effect of total flux expansion, leaving the upstream roll-over density the same. Said another way, recycling neutrals are more likely to be ionized, and ionized near the separatrix flux surface, for the low-R_t case than for the high-R_t case.

2.2 Modelling of a TCV total flux expansion scan with SOLPS-ITER [30][31]

SOLPS-ITER includes a combination of the plasma fluid code B2.5 as well as an EIRENE [37] Monte-Carlo kinetic neutrals code operating using a grid that covers the plasma but also extends to surrounding walls (see analysis grids in Fig. 3).

We set the power entering the B2 grid from the core, and thus the power crossing the separatrix into the SOL, P_{SOL}, to be 600 kW for these simulations. This is comparable to the differences in experimental measurements of input power and power radiated inside the separatrix which gives a P_{SOL} range of $\approx 400-600$ kW. In terms of pumping and puffing, we use an effective wall pump by choosing a recycling coefficient of 0.99 at all the wall surfaces and the targets. The combination of the puffing rate (matching experiment), the recycling coefficient and the Carbon chemical sputtering at the wall (with a 3.5% yield) is chosen to qualitatively match experimental measurements from the Charge Exchange Recombination Spectroscopy (CXRS) [38] for the observed carbon content, the Thomson Scattering (TS) system for the upstream/midplane density and temperature profiles, the experimental puff rate range and the baratron gauge measurements of neutral pressure in the divertor and at the midplane. Radial transport is assumed to be diffusive and the transport coefficients are chosen to roughly match the experimental measurements of n_e (electron density) and T_e (electron temperature) profiles at the midplane for an attached case as measured by Thomson Scattering and the reciprocating Langmuir probe [39]. The transport coefficients are kept identical for all the simulations shown in this paper, with $D_\perp = 0.2\ m^2.s^{-1}$, $\chi_{e,\perp} = \chi_{i,\perp} = 1\ m^2.s^{-1}$. We will discuss this choice of transport coefficients and its impact on the results in the discussion section.

Using those inputs, we perform multiple SOLPS-ITER simulations approximating an upstream (separatrix) density scan, by modifying the D_2 puff rate for each simulation. All the puffed particles enter the grid at the position of TCV valve 1 ($R = 0.69m$, $Z = -0.74m$). Each of these simulations converges in about 10000 time

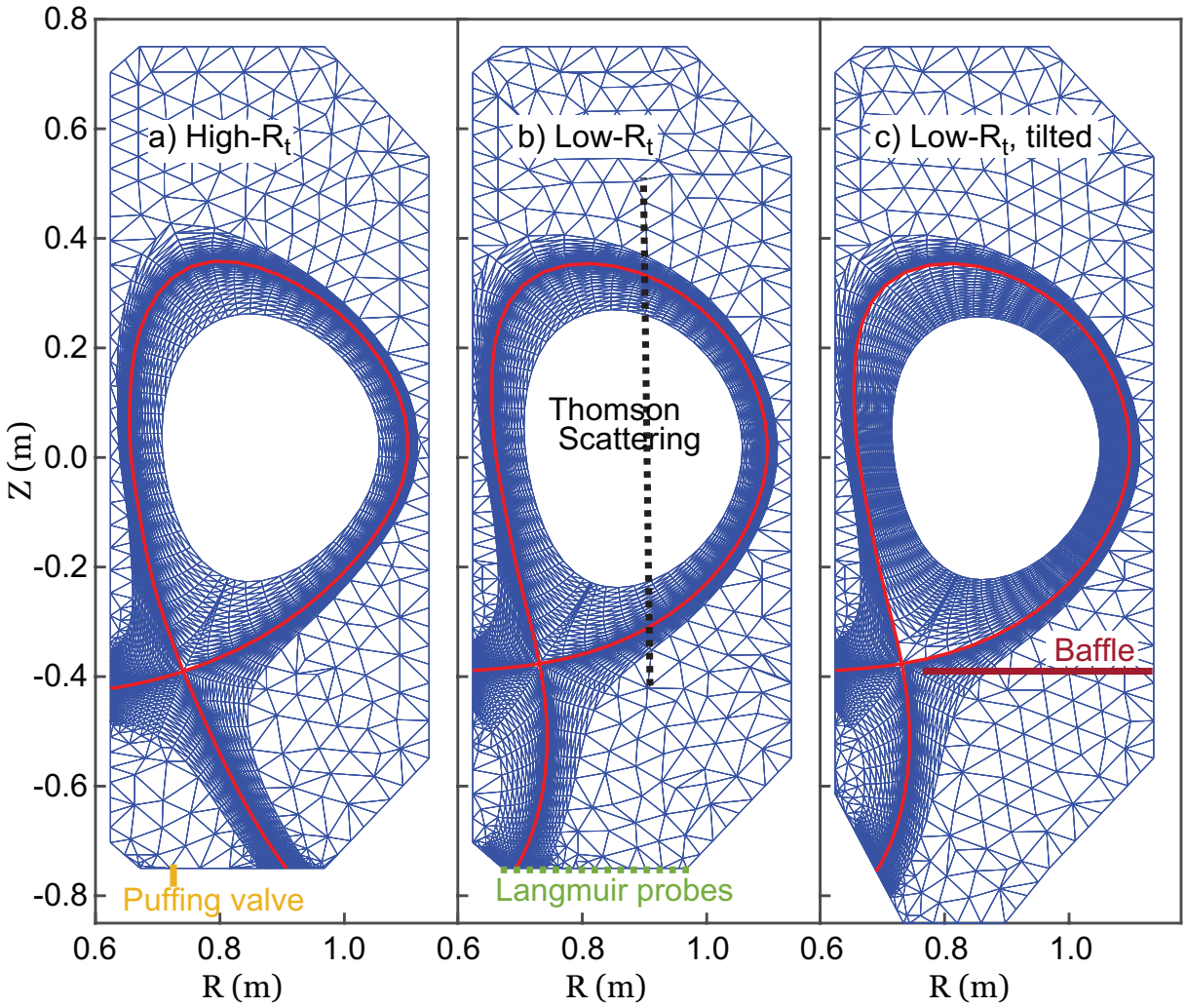

Figure 3: SOLPS-ITER grids for the different simulations presented in this paper: a) "High-R_t", b) "Low-R_t", c) "Low-R_t tilted". The EIRENE grids for kinetic neutrals extend towards the realistic TCV walls. The resolution of the B2 grids (plasma domain) are 86x38 ($\parallel \times \perp$, aligned on flux surfaces with the lowest mesh spacing near the targets and the separatrix). Also shown is the position of the Thomson Scattering measurement ($R = 0.9\ m$), the Langmuir probes which cover the outer divertor target, and the position of the gas valve from which we puff particles in the simulation. The position of the baffle-like surface used in section 3 is also shown.

steps of 10^{-5} s. Those steady state simulations are deemed to be converged when all quantities are constant with time and that the puffed neutral flux is equal to the pumped neutral flux ($\Gamma_{puffed} = \Gamma_{pumped}$). The range of upstream separatrix densities obtained in this set of simulations is $0.8 - 4.5 \times 10^{19}\ m^{-3}$, which is slightly larger than the range of upstream densities observed during experimental density ramps. Note that the puff rates are very similar to the experimental rates ($0.1 - 2.2 \cdot 10^{21}$ particles/s). As we increase the puff rate and thus the upstream density, simulations progressively reach a detached regime characterized by the rollover of the peak and total ion flux at the outer target and very low target T_e.

We first analyze the particle balance during a density scan of the high-R_t configuration. This analysis is

performed for a bundle of flux tubes which are near the separatrix where the target heat flux is peaked when the plasma is attached (see Fig. 4a). Approximately 25% of the total heat flux entering the divertor is carried within those flux tubes. The flux tubes closer to the separatrix are not included in the bundle because they are strongly affected by cross-field transport into the private flux region and we want to avoid that effect in a study of detachment. In the rest of the paper we will focus on those flux tubes (and their equivalent for the low-R_t configuration) when plotting the particle balance and the ion flux. In Fig. 4b we display all the contributing factors to the target ion current, $\Gamma_{target} = \Gamma_{upstream} + S_{ionization} + S_{recombination} + \Gamma_{Rad.transp.}$. Γ_{target} is the ion flux reaching the outer target, $\Gamma_{upstream}$ is the ion flux entering the flux tubes at the height of the X-point (top end of the red region) and is mainly caused by ionization upstream in the SOL. $S_{ionization}$ and $S_{recombination}$ are respectively the total ionization and the total recombination (three-body and radiative) sources in the computational flux tubes (toroidally integrated as well) below the X-point; the value is negative for the recombination as it is a sink of particles. $\Gamma_{Rad.transp.}$ is the net radial flux of particles out of the flux tubes below the X-point. It is positive if more particles are entering than leaving the domain, negative otherwise.

We observe that recombination is not a significant contributor to the rollover of the target ion flux at detachment onset, consistent with TCV experimental measurements by Verhaegh [35] and previous modelling of TCV [40]. The divertor ion source (S_{ion}) is predicted by SOLPS to be the primary source of the ion target current as in experiment [35]; both the ion source and the target ion flux roll-over as the upstream density is increased. From previous modeling and experiment we know that the ion source is limited by the power available for ionization [35] [40].

The simulated target profiles in attached conditions do not follow the predicted effect of total flux expansion, consistent with experiments [3]. Figure 5 displays the simulated target density, temperature and ion flux profiles at the target. The 'expected' high-R_t target profiles are scaled from low- to high-R_t assuming that total flux expansion was the only change between the two configurations (eq. 2), i.e. $(\Gamma_{target})_{expected} = (\Gamma_{target})_{low-R_t} \times (\frac{B_u}{B_t})_{high-R_t}/(\frac{B_u}{B_t})_{low-R_t}$, $(T_{e,target})_{expected} = (T_{e,target})_{low-R_t} \times ((\frac{B_u}{B_t})_{low-R_t}/(\frac{B_u}{B_t})_{high-R_t})^2$, and $(n_{e,target})_{expected} = (n_{e,target})_{low-R_t} \times ((\frac{B_u}{B_t})_{high-R_t}/(\frac{B_u}{B_t})_{low-R_t})^2$. These equations also assume that both low- and high-R_t configurations are attached with similar upstream profiles/-conditions - as was approximately true for the modelling (less than 5 % difference in the upstream density of those two simulations). The large discrepancy between simulated and expected high-R_t target profiles again

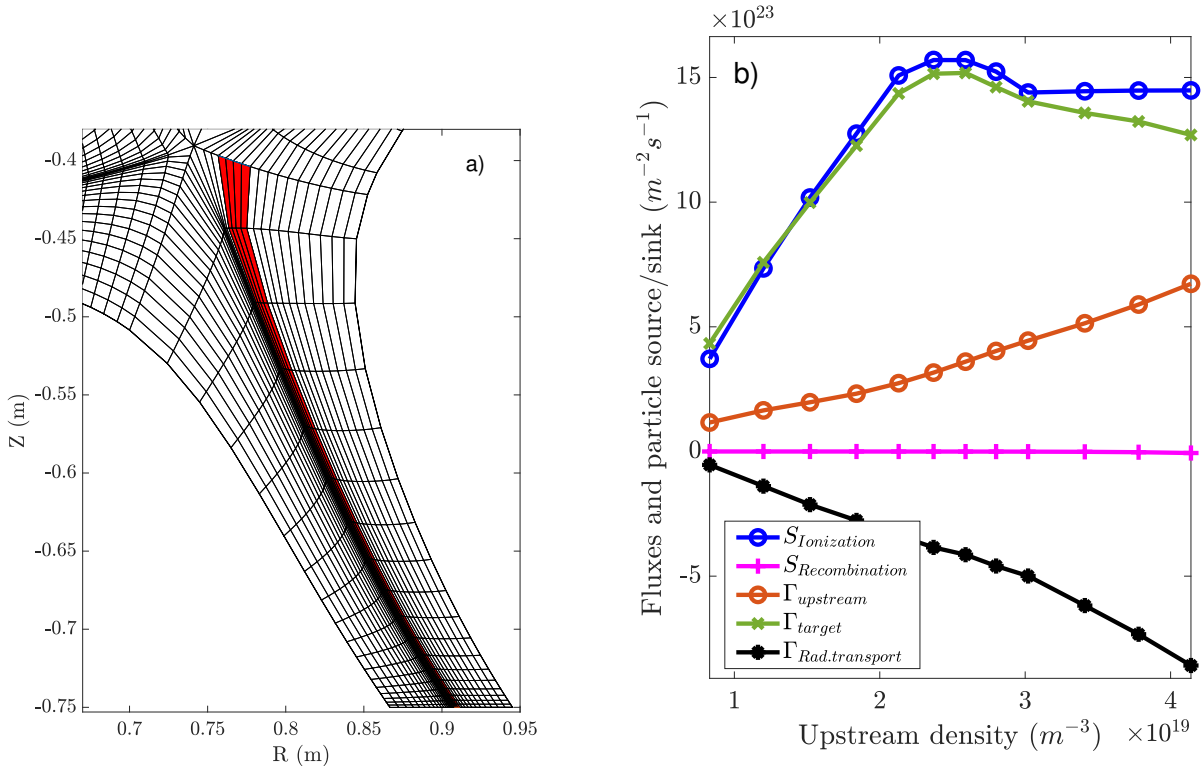

Figure 4: Analysis of the particle balance in a bundle of SOL flux tubes. a) Flux tubes (red domain) for which the target heat flux is peaked in attached conditions. b) Particle balance for the upstream density scan for the high-R_t case. Γ_{target} is the ion flux to the outer target (only at the end of the flux tubes), $\Gamma_{upstream}$ is the ion flux entering the flux tubes and is mainly caused by ionization upstream, $S_{ionization}$ and $S_{recombination}$ are respectively the total ionization source and the total recombination sink in the flux tubes, and $\Gamma_{Rad.transp.}$ is the net radial flux of particles out of the flux tubes. The rollover of Γ_t occurs for $n_{e_{up}} \approx 2.6 \times 10^{19} m^{-3}$.

suggests that an additional effect is counteracting the effect of total flux expansion in the simulations and in the experiments.

A clear demonstration of the low-R_t configuration having a lower upstream detachment density threshold than the high-R_t configuration is found when following the modelled evolution of the ion flux to the target for the two configurations during upstream density scans, Figure 6a.

The earlier detachment threshold for the low-R_t case is roughly consistent with the experimental results of Figure 2 as the low-R_t has a lower detachment threshold than the high-R_t. In addition, Fig. 6b shows that the target temperature for the low-R_t case is lower than that for the high-R_t at all upstream densities; the target temperature drops fastest as a function of upstream density for the low-R_t case.

The differences in detachment threshold between the two configurations are also echoed in the movement of the divertor impurity radiation (total radiation) from the target to the X-point, as can be seen in Figure 7. There is a similar delay between the total radiation front movements (Fig. 7) and the target ion flux rollover

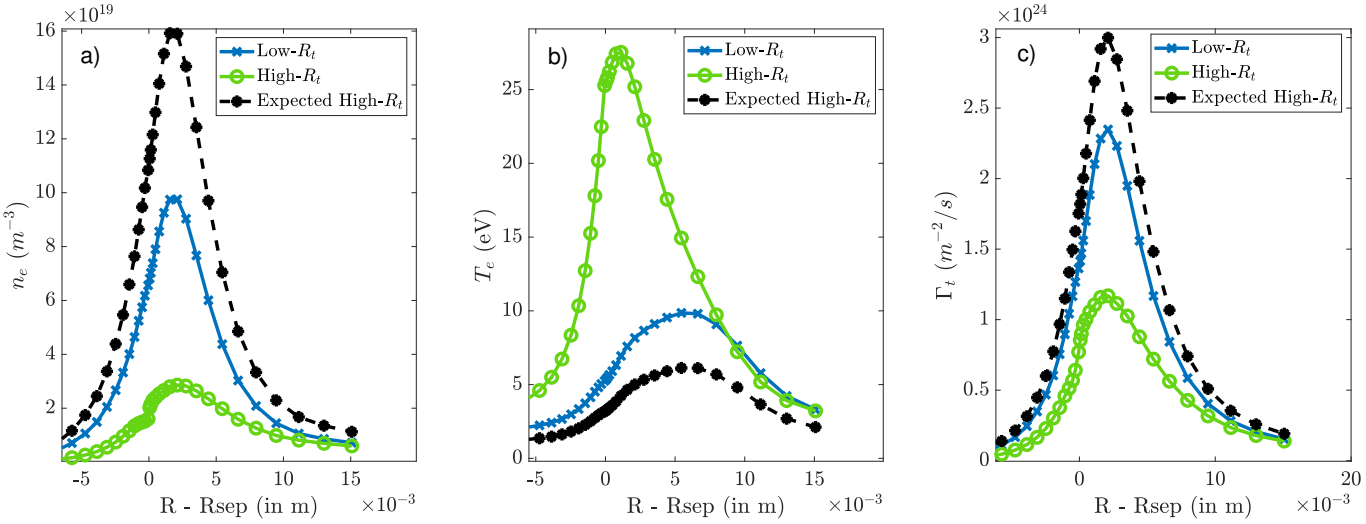

Figure 5: Target profiles of the a) electron density, b) electron temperature and c) ion flux for the Low- and High-R_t configurations. Both are in attached regime, with almost identical upstream profiles. Also shown is the expected target profiles of the high-R_t configuration scaled from the low-R_t profile if total flux expansion was the only factor changing in equation 2.

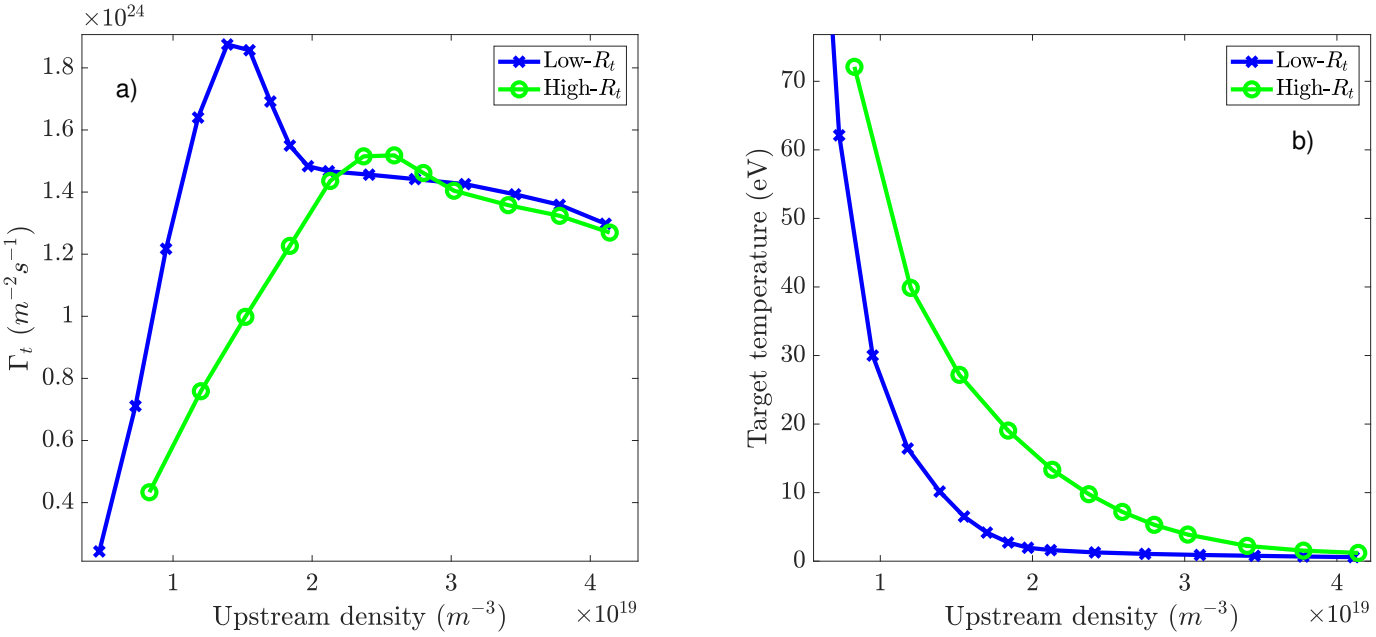

Figure 6: Evolution of the ion flux to the outer target (a) and the target electron temperature (b) of the flux tubes where the peak heat flux is in during the attached phase (see Fig. 4a), for the low-R_t and high-R_t configurations. The upstream density used is the midplane separatrix density.

for the low-R_t vs high-R_t cases (Fig. 6a). As similar delay in radiation movement (CIII emissivity) was found experimentally [41] for the two pulses in Figure 2 [3], it gives more confidence to the experimental value of N_{thres} of 0.85 between the two experimental cases.

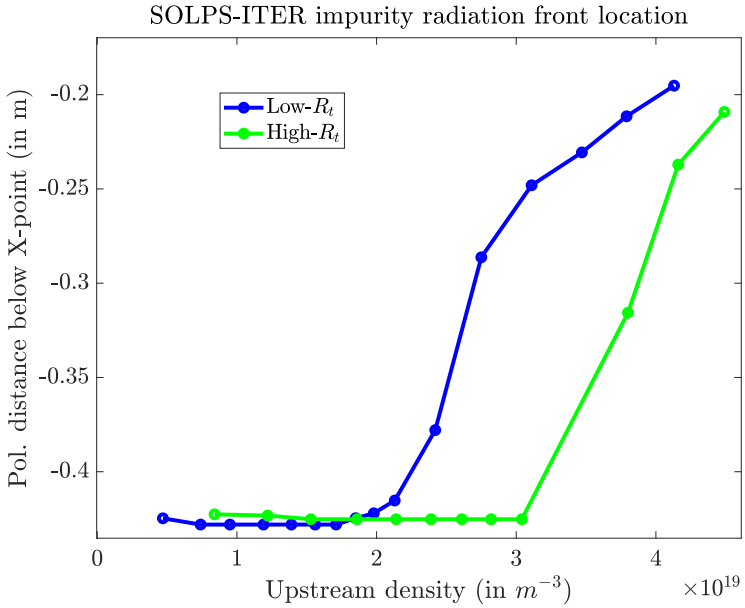

Figure 7: Movement of the total impurity radiation front edge (towards the x-point) in the SOLPS-ITER simulations as the upstream density is increased.

Both the SOLPS results shown in Figures 6 and 7 give $N_{thres} \sim 0.7$ instead of the expected total flux expansion scaling of $N_{thres} = 1.3$.

The next section will focus on our analysis of the simulations and code experiments which indicate that divertor geometry effects on neutral ionization are counteracting the effects of total flux expansion.

3 Effect of neutral trapping on the total flux expansion scan

3.1 Mechanisms which counteract the effect of total flux expansion in TCV

In an effort to understand what processes are counteracting the effect of total flux expansion in TCV, we have utilized the modified 2 point model formulation (2PMF) equations [4] [42] applied to the SOLPS outputs, as derived in [43]. The 2PMF description of the target ion flux, Γ_{tgt}, is given in equation 2 where γ_{sheath} is the sheath heat transmission coefficient, m_D is the mass of Deuterium, p_{tot} is the total upstream pressure, q_u is the upstream heat flux, $\tau_t = (T_i/T_e)_{target}$, $Z_t = (n_e/\sum n_{ion})_{target}$, M_t is the target Mach number, f_{mom}/f_{pwr} are the fraction of momentum/power lost between upstream and the target and B_u and B_t are the values of the total magnetic field at the entrance and the end of the flux tubes. The overall prediction

of the target ion flux calculated with this equation is extremely close to the direct code output for Γ_t (1% difference, not shown).

$$\Gamma_{tgt} = [\frac{\gamma_{sheath}}{8 \cdot m_D}] \cdot [\frac{p_{tot}^2}{q_u}] \cdot [\frac{2}{1+\tau_t/Z_t}] \cdot [\frac{4 \cdot M_t^2}{(1+M_t^2)^2}] \cdot [\frac{(1-f_{mom})^2}{(1-f_{pwr})}] \cdot [(\frac{B_u}{B_t})] \tag{2}$$

We have compared the ratio of the factors surrounded by square brackets in equation 2 for the high-R_t and low-R_t cases. We find that most of the terms of equation 2 are similar between the two different configurations under similar upstream conditions (same $n_{e_{up}}$ in both low-R_t and high-R_t). The exceptions are the total flux expansion term $(\frac{B_u}{B_t}) = f_R$ (expected) and the power and momentum losses term $\frac{(1-f_{mom})^2}{(1-f_{pwr})}$.

Going a step further and decomposing the different power sources and sinks in the code, we find that the main differences in the power losses between the two R_t configurations can be traced to impurity and hydrogenic radiation. In both cases, impurity radiation contributes to $\sim 50\%$ of the total power losses and hydrogenic radiation to $\sim 35\%$ of it. The rest of the power losses are due to molecules-plasma interactions.

Interestingly, when density scan simulations are performed without Carbon in the plasma (so no power sink from impurity radiation), the low-R_t case still detaches before the high-R_t case (both at higher upstream densities than their equivalent cases with Carbon) and the difference in power losses between configurations changes to a difference of hydrogenic radiation only (i.e. the qualitative difference between configurations is insensitive to the impurity model used). This points to an increased ionization in the low-R_t case compared to the high-R_t case which could lead to higher C radiation losses (when C is included) through higher densities. The increased power losses in the low-R_t configuration are also correlated with a higher neutral content (sum of all atoms and molecules in the divertor) in that divertor plasma compared to the high-R_t configuration. All those observations are consistent with the hypothesis that there is an increased neutral trapping in the low-R_t case than in the high-R_t case.

We have developed a measure of neutral trapping shown in eq. 3.

$$\eta_{RI} = \frac{S_{ion,ft}}{\Gamma_{t,tot}} \tag{3}$$

$\Gamma_{t,tot}$ is the total outer target ion flux (within the plasma grid) and $S_{ion,ft}$ is the ionization source integrated in the 4 flux tubes considered (from the entrance of the divertor to the target, as shown in Fig. 4a) coming from neutrals *originating from the outer target only*. The parameter η_{RI} is thus a measure of how

well outer divertor recycled neutrals are re-ionized in that divertor leg instead of escaping. Based on Fig. 8, we indeed observe a larger η_{RI} (higher neutral trapping) in the low-R_t case. We note that in both cases η_{RI} increases and peaks before the target ion flux rollover, and then decreases as detachment proceeds (see Figure 6a). Since the calculation of η_{RI} is normalized to the target ion flux, the rise, peaking, and then fall of η_{RI} is likely linked to the changes in ionization mean free path of recycled neutrals - $\lambda_{mfp,ion}$ - which first shortens, reaches a minimum before detachment and then rises after detachment; a larger $\lambda_{mfp,ion}$ would mean that recycling neutrals more easily escape the plasma fan.

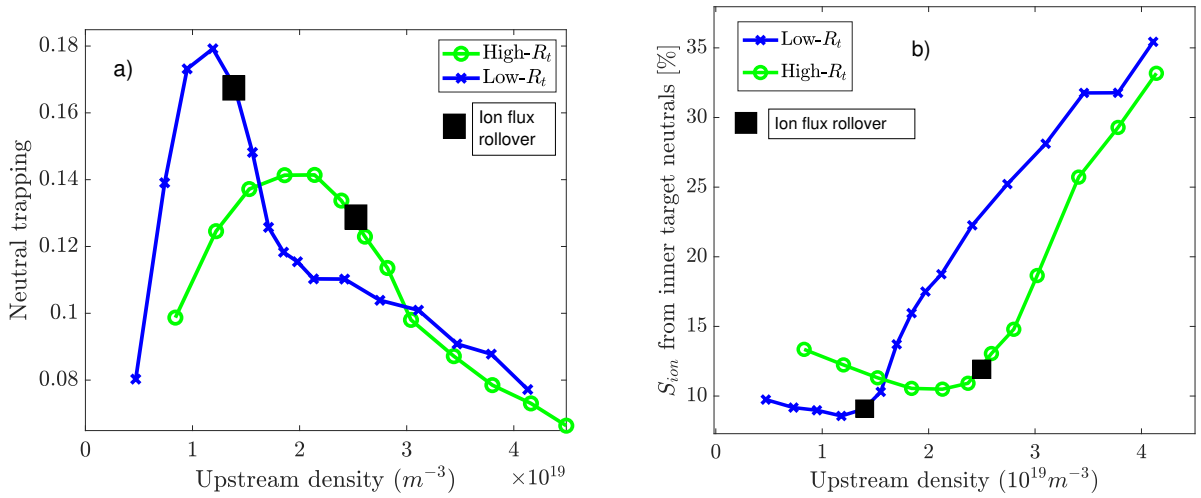

Figure 8: a) Measure of the neutral trapping, η_{RI} (eq. 3), as the fraction of neutrals *originating at the outer target* which ionize in a set of outer divertor flux tubes below the x-point (highlighted in red in Fig.4a). b) The ionization (percentage) occurring in the highlighted outer divertor flux tubes due to neutrals originating from the inner target.

There are several differences between the neutral pathways between the two R_t configurations which could explain this difference in neutral trapping. In particular we can point to advantages of the low-R_t configuration compared to the high-R_t configuration:

a) The strike-point in the low-R_t case is located near the inner wall which helps confine neutrals near the target.

b) The strike-point (poloidal) angle with the target for the low-R_t would tend to direct recycled (and reflected) neutrals more towards the separatrix and the private flux region as opposed to the high-R_t case where the strike-point angle would generally direct recycled (and reflected) neutrals into the main SOL.

The second effect (b) of the strike-point angle affecting the density detachment threshold has already been studied experimentally in a comparison of 'vertical-target' (sending more neutrals back towards the separatrix) vs 'horizontal-target' divertors (sending more recycling/reflected neutrals towards the common flux region) for the first vertical target divertor [15] [26]. Operation on the vertical target led to a 40% reduction in the density detachment threshold compared to the horizontal target; the study pointed to enhanced power losses for the vertical target as the reason. The authors further speculated that the enhanced losses were due to the fact that 'recycling neutrals are aimed back at the separatrix for all points' in the divertor. More recently, EDGE2D has also been used to study the underlying physics of the lower detachment threshold in JET with vertical target. Neutrals, recycling direction and geometry were clearly shown to play a central role in the lower detachment threshold [27].

The above two effects (a and b), which tend to lower the detachment threshold, are combined for the low-R_t case given that the recycling neutrals are generally launched towards the separatrix (effect b) and then return towards the separatrix as the inner wall reflects them back (effect a); the inner divertor leg limits their loss to the midplane. And clearly, for the high-R_t configuration, those advantages do not exist: the recycling neutrals are generally launched away from the separatrix towards the far SOL (effect b) and then there is no close fitting wall to reflect them back towards the plasma fan, nor a baffle to keep them from escaping to the midplane (effect a).

Neutrals generated at the inner target can also be ionized in the outer divertor leg fan. We do not include them in the calculation of η_{RI} as they do not originate from the outer divertor and thus don't qualify as being 'trapped' in the divertor leg where they originate. Even if we did include those neutrals originating from the inner divertor, they would only be responsible for less than 12% of the ionization occurring in the outer divertor before and at the rollover, and contribute similarly in both configurations.

To confirm these conjectures above about the role of neutral trapping, we now present "experiments in the code" to modify the neutral trapping properties of the two divertor configurations.

3.2 Effect of the strike-point angle on neutral trapping and TCV detachment

To investigate the second effect outlined above, we have created and studied a modified low-R_t case, designed such that the angle between the outer divertor leg and the target (strike-point angle) is now exactly the same as in the high-R_t case. This angle change should aim more recycled neutrals away from the separatrix. This was achieved by tilting the existing TCV wall for the low-R_t case, as shown in the third plot of Figure 3.

We designate this configuration as "Low-R_t tilted". Consistent with our expectations, the target ion current

rollover occurs at a higher upstream density than the normal low-R_t scan, and slightly higher than in the high-R_t configuration (Figure 9a). Also as expected, the neutral trapping peaks at a higher upstream density and the value of neutral trapping is reduced (see Figure 9b). In terms of the ratio of upstream density at rollover, N_{thres}, the value changes from ~ 0.7 (Low-R_t vs. High-R_t) to ~ 1 (Low-R_t tilted vs. High-R_t), thereby closer to the predicted scaling for the effect of total flux expansion only (i.e. 1.3).

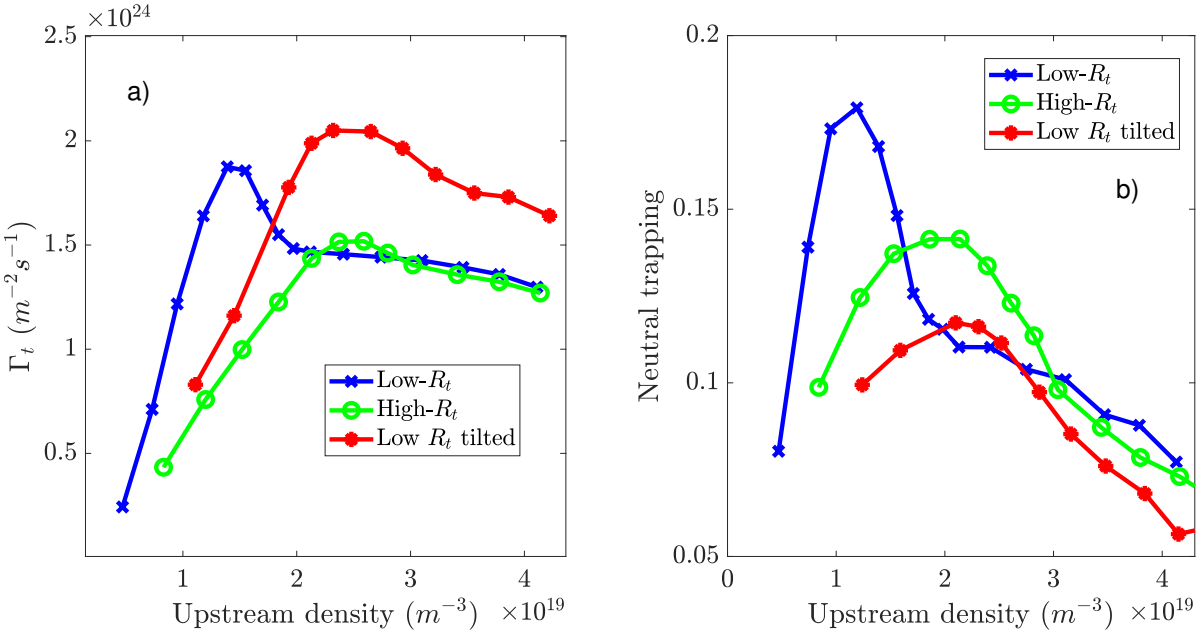

Figure 9: Evolution of the ion flux to the outer target (a) and the neutral trapping, η_{RI} (b), of the flux tube where the peak heat flux is during the attached phase (see highlighted flux tubes in Fig. 4a), for the Low-R_t, High-R_t and Low-R_t tilted ('horizontal-target') configurations.

Thus, by using the same strike-point angle for both configurations, low- and high-R_t, we partially recover the total flux expansion effect on TCV; said another way, we have reduced the neutral trapping non-uniformity between low- and high-R_t. Note that this change of geometry also introduces extra wall area (roughly 8%) in the divertor which increases the pumping slightly given that the recycling coefficient on the walls is less than 1. We don't feel that this additional pumping is significant in the results.

3.3 Effect of complete divertor neutral baffling on TCV detachment

Our second modification of the neutral trapping addresses the first effect (a) outlined earlier. The goal is to make the overall neutral trapping in the divertor more uniform between the low- and high-R_t configurations by strongly limiting the ability of neutrals to escape to the SOL above the X-point. This is achieved through

the addition of a baffle-like structure as shown on Figure 3c for both low- and high-R_t configurations. Note here that the baffle is designed to act only on the neutrals, not on the plasma, reflecting the neutrals back into the divertor. This addition of the baffle is primarily to enhance the neutral trapping of the high-R_t case given that the neutrals in the low-R_t configuration tend to be already trapped between the separatrix, the main plasma and the inner wall - in the private flux region.

A density scan through detachment was repeated for both low-R_t and high-R_t configurations with baffles. The results are shown in Figure 10. The additional baffle structure considerably increases the magnitude of neutral trapping for the high-R_t case. This is in contrast to the low-R_t case where the neutral trapping value is relatively unchanged - the neutrals that end up in that region are already fairly well trapped. The baffling thus effectively homogenizes the overall neutral trapping between the two configurations. The detachment density threshold for the high-R_t case shifts significantly to lower densities. This is expected given how poorly neutrals are trapped in that configuration. The density detachment threshold for the low-R_t case does slightly shift to lower upstream densities as well (figure 10a) and the value of N_{thres} for the two baffled cases rises to slightly above 1. This is consistent with recent modeling of the TCV baffle upgrade which also finds a large detachment threshold drop with the addition of a baffle [44]. Note that the puff rate for all configurations must be increased to reach the specified upstream density.

The above variations in baffling and strike-point angle are each treated separately to better delineate their effects on neutral trapping and on the upstream density detachment threshold. We next complete our efforts to equalize the effects of divertor geometry between low- and high-R_t by combining baffling and using the same strike-point angle for both configurations.

In this final case - Low-R_t tilted baffled, the neutral trapping peak value drops compared to the low-R_t baffled. Both the rollover in η_{RI} and the target ion flux shift to higher upstream densities (Fig. 11a and 11b). The N_{thres} based on the results in Fig. 11a, rises to ~ 1.48, even beyond that predicted for total flux expansion, 1.3. The target profiles for the baffled cases in attached conditions are consistent with the higher N_{thres} than 1.3, with a significantly higher target density ($\sim 1.5^2$ higher) in the high-R_t baffled configuration (i.e. much lower target temperature) than in the low-R_t tilted baffled configuration, for similar upstream conditions (see Figure 12). The temperature and ion flux profiles shift approximately by $1/(1.5)^2$ and $1/1.5$, respectively, between low- and high-R_t. The 2PMF analysis of section 3.1 is also consistent with the changes in N_{thres} resulting from the comparison of low-R_t tilted-baffled with the high-R_t baffled. The power and momentum loss term $\frac{(1-f_{mom})^2}{(1-f_{pwr})}$ from the 2PMF changes from 0.3, with the actual TCV geometry, to 1.1,

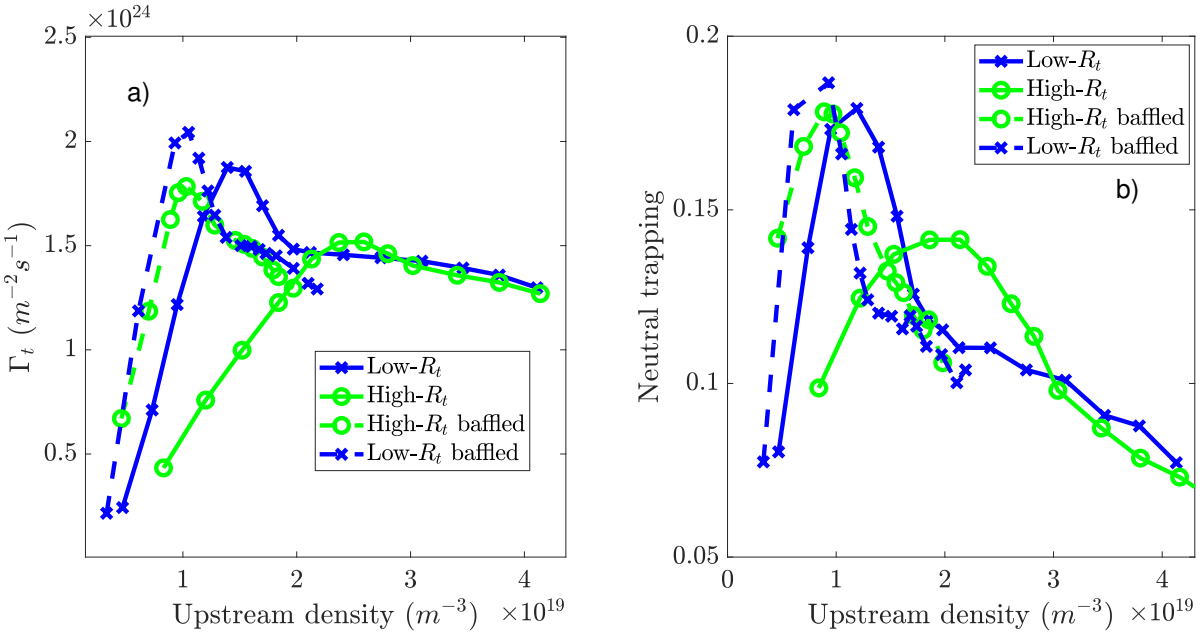

Figure 10: Evolution of the ion flux to the outer target (a) and the neutral trapping, η_{RI}, of the flux tube where the peak heat flux is in during the attached phase (b), for the Low-R_t, High-R_t, Low-R_t baffled and High-R_t baffled configurations.

where 1 would indicate no change. As expected, the total flux expansion term (1.3) is the dominant term. From the 2PMF result and N_{thres} rising above 1.3 it appears we have somewhat overcompensated in our efforts to make the low-R_t case more similar to the high-R_t case from the point of neutral trapping; the ratio of the N_{thres} obtained (1.48) to that predicted (1.3) is close to the ratio of the power and particle balance term $\frac{(1-f_{mom})^2}{(1-f_{pwr})}$ for the low-R_t tilted-baffled to the high-R_t baffled - 1.1.

4 Discussion

4.1 Sensitivity of SOLPS results to the choice of transport coefficients

In this work we studied the effect of varying the transport coefficients on the 'best' match to TCV data. Our initial criteria were to match the upstream and target profiles of density and temperature. The results for the transport coefficients ultimately used in the study are given in Figure 13. The match to the upstream density and temperature profiles is not optimal, nor the match to the target profiles. The target ion flux is overestimated by a factor $1.5 - 2$. This overestimation occurs for both low-R_t and high-R_t configurations.

A better match to the upstream and target profiles has been obtained by increasing the SOL $D_\perp$ by a factor 10. The lower value of $D_\perp$, used for the cases in this paper, is 0.2 $m^2.s^{-1}$ and the higher value

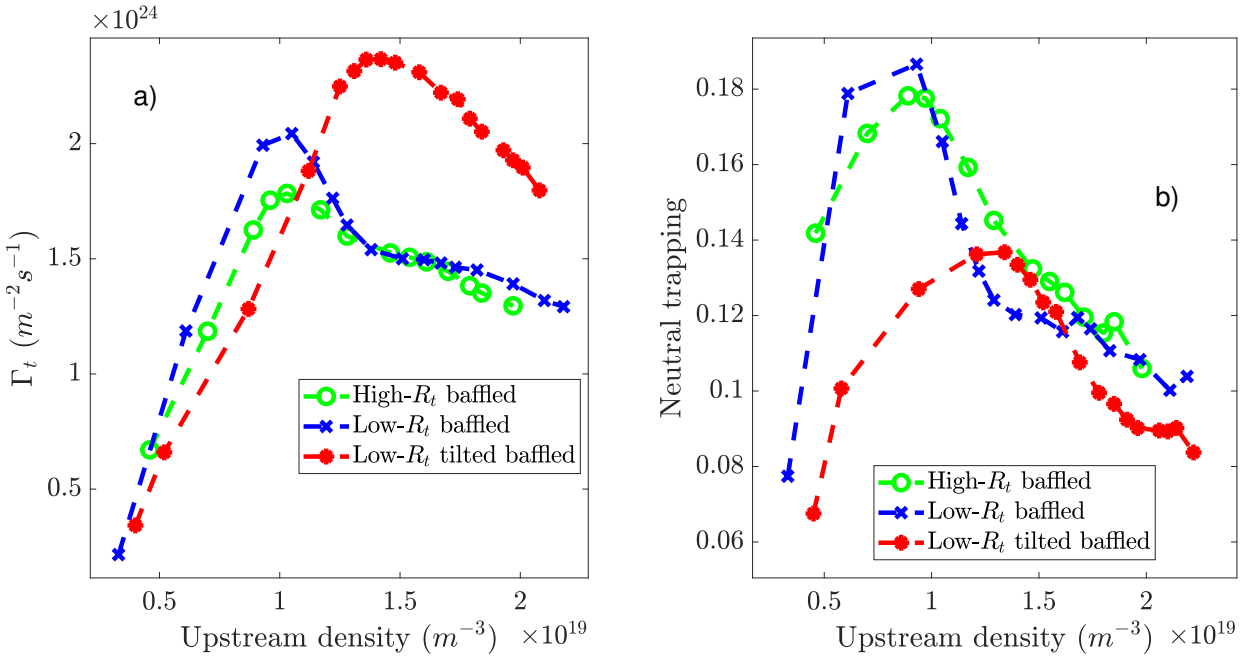

Figure 11: Evolution of the ion flux to the outer target (a) for density scans with a baffle-like structure. The high-R_t baffled rolls-over at lower upstream density than the low-R_t baffled, and the ratio of detachment thresholds between the low-R_t tilted baffled and the high-R_t baffled is much closer to the total flux expansion scaling. The low-R_t tilted baffled configuration rolls-over at significantly higher upstream density than the high-R_t baffled. Also shown is the neutral trapping for these three cases (b).

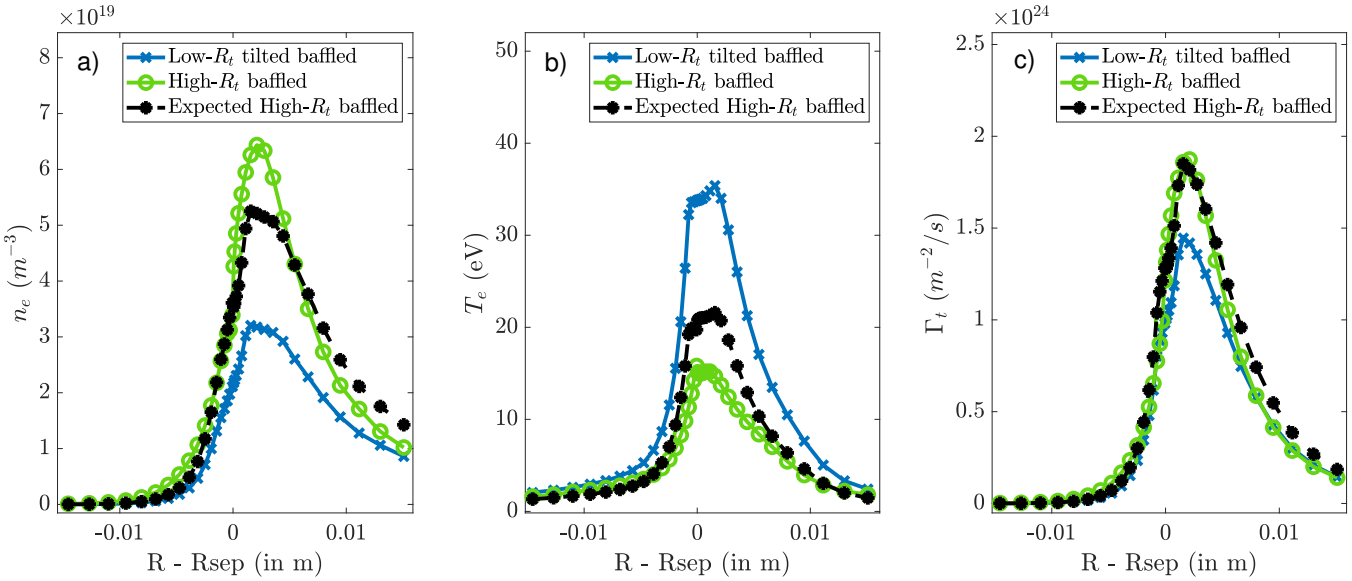

Figure 12: Target profiles of the a) electron density, b) electron temperature and c) ion flux for the Low-R_t tilted baffled and High-R_t baffled configurations. Both are in attached regime, with almost identical upstream profiles. The 'expected' values are scaled by the model prediction value, 1.3.

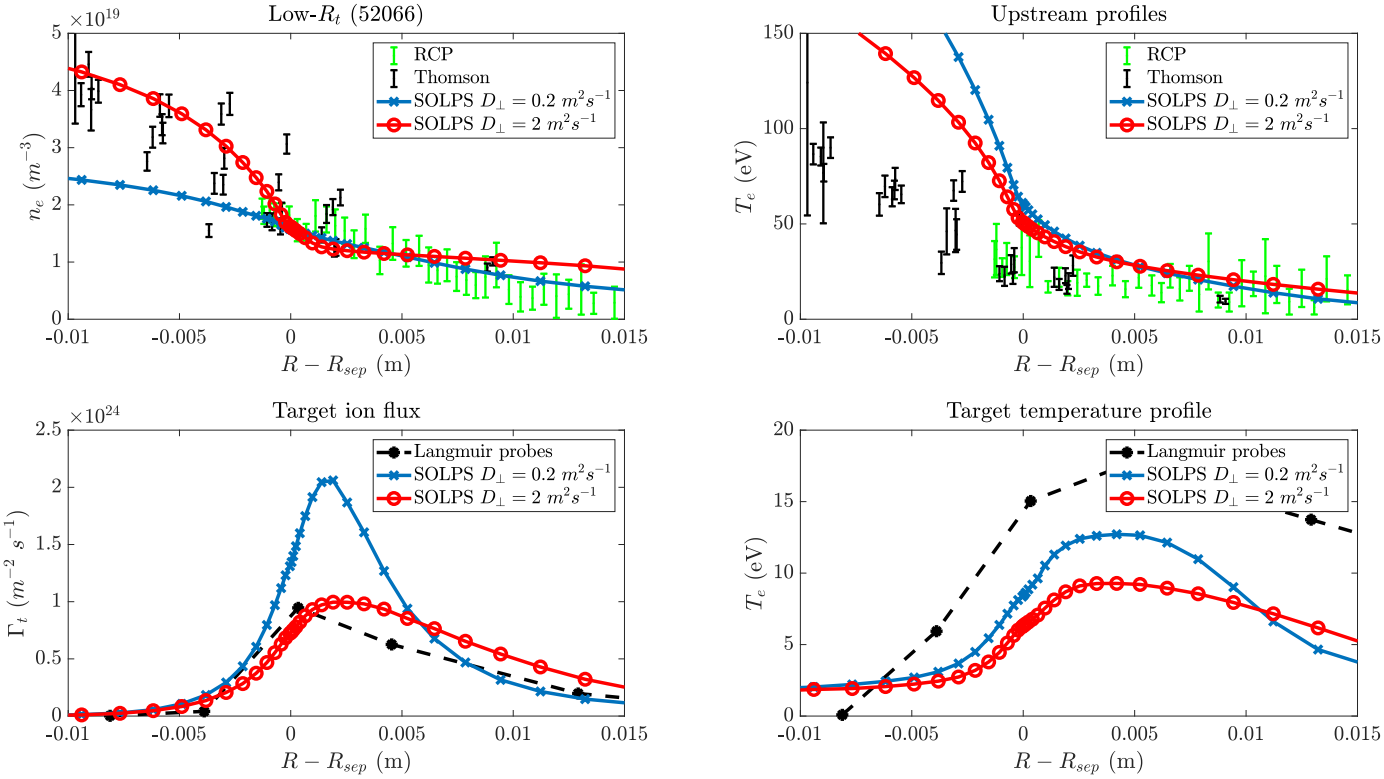

Figure 13: Comparison between experimental upstream n_e and T_e profiles from TS and RCP for an estimated upstream density of $\sim 1.4 \times 10^{19}\ m^{-3}$, and SOLPS-ITER-predicted profiles for a D_2 puff rate of 5×10^{19} part/s and two different particle diffusivities. Both cases have $D_\perp = 0.2\ m^2 s^{-1}$ in the core region. In the SOL, the simulation in blue also has $D_\perp = 0.2\ m^2 s^{-1}$ while the simulation in red has an increased $D_\perp$ ($= 2\ m^2 s^{-1}$) in the SOL.

tested was 2 $m^2.s^{-1}$ (only increased in the SOL). The higher diffusion coefficient increased radial transport through the radial limits of the SOLPS grid leading to a reduction in the target ion flux to values similar to experimental ones (at least for the ion flux, as can be seen on Figure 13).

However, this improved agreement at high values of the transport coefficients came at the cost of an implausibly high electron temperature at rollover (of the total target ion flux) of 10 eV, compared to $1 - 2$ eV for the simulations with a flat $D_\perp = 0.2\ m^2.s^{-1}$ profile. This high rollover temperature is not due to a drop of the particle source (ionization) or an increase of the sink at 10 eV. Rather the decrease in target ion flux is due to the strongly increased radial flux and loss of particles out of the simulation domain; the enhanced loss of ions radially out of the grid is most pronounced on the private flux region side, extending to flux tubes in the common flux region. We note that this nonphysical domination of the roll-over by radial losses out of the grid could not be "fixed" by extending the grid radially given the size of the TCV chamber and the equilibrium considered. The above issues drove us to choose the lower diffusivity used in this paper.

Over the range of diffusivities utilized, the ratio of density thresholds for detachment between configurations changes slightly ($N_{thres} = 0.8$ instead of 0.7 when the diffusivity is increased is the SOL) but the qualitative results and conclusions of the paper do not seem to depend on this choice of diffusivities, at least for the three different values tested (simulations with $D_\perp = 1\ m^2.s^{-1}$ were also performed but not shown here). A summary of the changes induced by a change of $D_\perp$ are shown in the table below.

Sensitivity scan to SOL $D_\perp$	0.2 $m^2 s^{-1}$	2 $m^2 s^{-1}$
N_{thres}, Low-R_t/High-R_t	0.7	0.8
N_{thres}, Low-R_t baffled/High-R_t baffled	1	1.1
Target temperature at rollover of total Γ_t	1-2 eV	10-15eV
Flux of electrons leaving the plasma grid (midplane to target)	4.4×10^{20} part/s	3.8×10^{21} part/s

A second difficulty encountered in the SOLPS predictions is their poor match with experimental data at the inner target. This was demonstrated/discussed in [40], and we believe that to enhance the agreement of the power sharing between outer and inner divertors, we would have to perform SOLPS-ITER simulations with drifts and ballooning-like diffusivities, the former of which was challenging and unsuccessful so far. The inclusion of poloidally-varying diffusivities ($= D_\perp \times B^2$) was tried and was not, by itself, enough to recover the inner-outer divertor asymmetry.

4.2 Interpretation of the overall TCV modelling study of magnetic topology and divertor geometry

In our efforts to understand and explain the observed lack of effect of total flux expansion on the upstream density detachment threshold in TCV, we feel we have demonstrated that neutral effects can dominate over total flux expansion. Since the topology and geometry effects are fairly independent, it means that all effects can be optimized independently to maximize the ability to detach the divertor even as both the upstream temperature and the collisionality drop while P_{SOL} is increased in reactor-relevant conditions - all of which make detachment more difficult. We bring together all the variations in baffling, strike-point angle and total flux expansion included in this paper in figure 14 to both illustrate and discuss the relative effects of the various variations.

Low-R_t configuration:

a) Low-R_t - recycling neutrals are generally aimed towards the outer separatrix leg, some ionized there and the remainder passing through to the inner wall which is fairly close. Some fraction of neutrals incident on the inner wall are reflected back towards the outer separatrix to enhance ionization. The inner separatrix can also contribute neutrals created by incident ions.

b) Low-R_t tilted - Outer divertor leg recycling is aimed away from the separatrix and towards the open chamber.

c) Low-R_t baffled - Same as the low-R_t but even the recycling neutrals travelling towards the common flux region are retained in the divertor by the baffle.

d) Low-R_t tilted baffled - Same as the low-R_t tilted but any neutrals that escape towards the common flux region are retained in the divertor by the baffle.

High-R_t configuration:

- High-R_t - recycling is aimed away from the separatrix and towards the open chamber
- High-R_t baffled - Same as the high-R_t but any neutrals that escape towards the common flux region are retained in the divertor by the baffle.

The detachment threshold in upstream density can be varied by a factor of 2.6 when considering the complete range of magnetic topology changes and divertor geometry explored in this study. However, given the small expected effect of total flux expansion on the detachment threshold in TCV (factor 1.3), the effect of divertor geometry and thus neutral trapping is dominant for TCV in determining the detachment threshold; larger variations in total flux expansion (2-3), and thus larger variation in detachment thresholds, will only be available in MAST-U [28].

Figure 14 also indicates that changing the strike-point angle has a different effect on the detachment threshold than a change of divertor closure (in this case the addition of the baffle). The tilt of the target which defines the Low-R_t tilted case aims the centroid of recycling neutrals away from the separatrix and towards the far SOL, switching from so-called "vertical" to the "horizontal target" orientation. This strongly reduces neutral trapping (η_{RI}) for the two cases where it was implemented. Note that this effect could be over-estimated in this study as the low-R_t tilted not only sends recycling neutrals towards the common flux region, but also adds wall surface that would increase the pumping of neutrals compared to the standard case.

In contrast to changing the target strike-point angle, baffling the entire divertor leads to lesser effects on

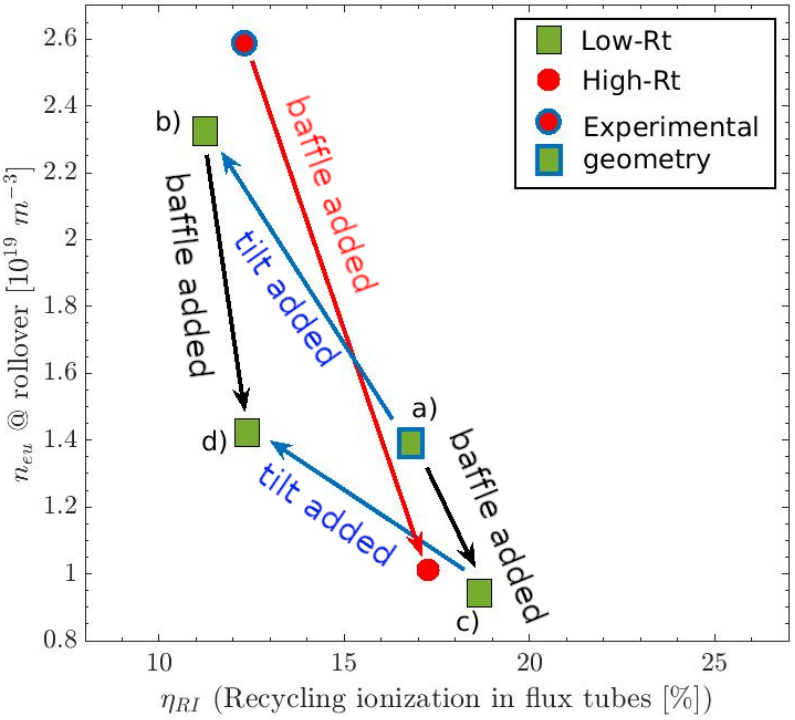

Figure 14: The relationship between n_{eu} at the target ion flux rollover and the percentage of the target ion flux ionizing in the flux tubes studied, η_{RI}. The four Low-R_t cases (green squares) are labelled as described in the text.

η_{RI} than tilting, as well as lesser effects on the density detachment threshold . We speculate that baffling raises the neutral ionization everywhere, an affect on the numerator and denominator of eq. 3. On the other hand, changing the strike-point angle would seem to affect the ionization in the flux tubes of interest but not change the overall ionization very much. As for the neutral trapping, the modifications of strike-point angle seems to have a larger effect on the detachment threshold than the baffling, at least for the low-R_t (which is already quite well baffled by its proximity to the inner wall). At the moment there is no obvious reason to choose one geometry change over the other. The maximal effect on the detachment threshold is produced when both effects are optimized, and optimized along with total flux expansion.

We postulate that all of the divertor geometry or magnetic topology changes investigated in this paper ultimately have the same effect - achieving about the same divertor density and temperature, n_{et} and T_{et} for detachment, but at a lower upstream density n_{eu}. For the divertor geometry variation cases this appears to be achieved through more neutrals being available and ionized (across the divertor for overall baffling and only on important flux tubes for the strike-point angle changes), which raises n_{et} and lowers T_{et}, the latter through more hydrogenic and impurity radiation.

The lowering of the upstream density detachment threshold through moving the strike-point to larger major radius at least starts through a different pathway than the increase of neutral density. When the strike-point is placed at a larger R_t the magnitude of the magnetic field at the target, $|B_t|$, decreases ($\propto 1/R_t$) and, due to conservation of magnetic flux, the flux tube area, A_t, increases ($\propto 1/|B_t|$). Conservation of the local heat flow through the flux tube, $q_{\parallel,t}A_t$, lowers $q_{\parallel,t}$. Through pressure conservation in attached plasmas, $T_{et} \propto (B_t/B_x)^2$, as described in the introduction. One implication of the data in Figure 14 is that tilting the strike-point to target orientation of the high-R_t case from 'horizontal' to 'vertical' would lead to even lower detachment thresholds for either the baffled or the unbaffled case.

What we have not addressed in this study are the effects of magnetic topology and divertor geometry on other characteristics of detachment. Those include a) He enrichment/pumping which is important for core fusion reaction dilution; b) impurity compression which when maximized, reduces the effect on the core plasma for the same level of impurities seeded in the divertor (to reduce target power loads); and c) control of the detachment location or depth. The above list is not meant to be exhaustive. However, one hopes that future studies of variations of divertor topology and geometry address more than the detachment threshold. We do note that changes in magnetic topology are predicted to improve control of the detachment location for an X-divertor [20] or a Super-X [21].

4.3 Effect of non-constant C_Z and upstream parallel heat flux ($q_{u,\parallel}$) on the total flux expansion scaling

While the focus in this paper has been on scanning just the upstream density, n_{eu}, though detachment for the different configurations, the reality is that as n_{eu} is varied, other characteristics of the SOL are also indirectly varied. For example, changes in n_{eu} and thus the target density lead to changes in the impurity fraction in the divertor, C_Z, due to variations in the sources (chemical sputtering) as well as forces on impurities along the field. Increasing n_{eu} also enhances cross-field transport ($n\chi\nabla T + TD\nabla n$) which, for constant P_{SOL}, lowers the upstream parallel heat flux, $q_{u,\parallel}$. In the following we examine the effect of the density scan on the impurity fraction in the divertor, C_Z and the upstream parallel heat flux, $q_{u,\parallel}$, and their roles in the detachment threshold.

As mentioned in the introduction, the contributions of the three different control variables n_{eu}, C_z, $q_{u,\parallel}$ to detachment are predicted in a study of the detachment location sensitivity [8]. Equation 27 of that study

is derived by explicitly including impurity radiation (based on the Lengyel formulation [45]) in the energy balance. The characteristics of the divertor magnetic topology are also included through the total field magnitude profile along the field line (total flux reduction or expansion) and the length of the field line in the divertor, L_{div}, as well as the overall connection length from target to upstream, L. That model is aimed generally at the detachment location movement from target to the x-point. For this paper we are only interested in the start of detachment at the target which predicts the detachment threshold of the form (simplified for this paper):

$$\frac{n_{eu} C_Z^{1/2}}{q_{u,\parallel}^{5/7}} = \frac{B_t}{B_X} f(B_t/B_X, l_{div}/L) \tag{4}$$

The right hand side (RHS) of this equation is a constant set by the magnetic topology of the divertor leg through B_t/B_X and L_{div}/L (assuming that impurity transport does not change). Thus, the product of the three terms on the LHS of eq. 4 at detachment are fixed by the divertor magnetic topology (this model does not include neutral effects). For example, while keeping the LHS constant, detachment can be reached at high n_{eu} and low C_Z or the opposite. We will now use eq. 4 as our prediction of the detachment threshold variation from low- to high-R_t of the combined detachment control parameters in the case of total flux expansion only. Figure 15 displays the variation of C_Z in the divertor with increasing n_{eu} for the 6 configurations. Since C_Z varies along a field line we have defined it to be the average value over the radiating region; this roughly corresponds to the model where C_Z is a constant over the radiating region in the divertor. As n_{eu} is increased and the divertor becomes more strongly recycling (before rollover), $C_{Z,div}$ drops strongly. Past roll-over the concentration rises again. In this study we focus on the $C_{Z,div}$ (as well as n_{eu} and $q_{u,\parallel}$) at roll-over (marked in the figure) as we are using that point as the start of detachment. At rollover, $C_{Z,div}$ is found to be between 0.77% and 1.58% across the various density scans for different divertor configurations; remember that $C_Z^{1/2}$ is utilized in eq. 4. It is slightly higher in the high-R_t configuration than in the low-R_t configuration, the two experimental configurations. The relatively higher concentration for the high-R_t case is consistent with the results shown in Figure 16 where the main power losses at rollover are given. Impurity radiation is the dominant power loss for both configurations and is higher in the high-R_t case.

We also review the variation of $q_{u,\parallel}$ across the various configurations at roll-over. As mentioned above, $q_{u,\parallel}$ drops slowly during density scans as n_{eu} increases; the value of $q_{u,\parallel}$ at detachment varies by $\sim 10\%$ from the lowest to highest n_{eu} across the various configurations, and $q_{u,\parallel}$ is higher in the low-R_t than in the high-R_t case. A higher $q_{u,\parallel}$ would require a higher n_{eu} or $C_Z^{1/2}$ to achieve detachment, as the right hand side

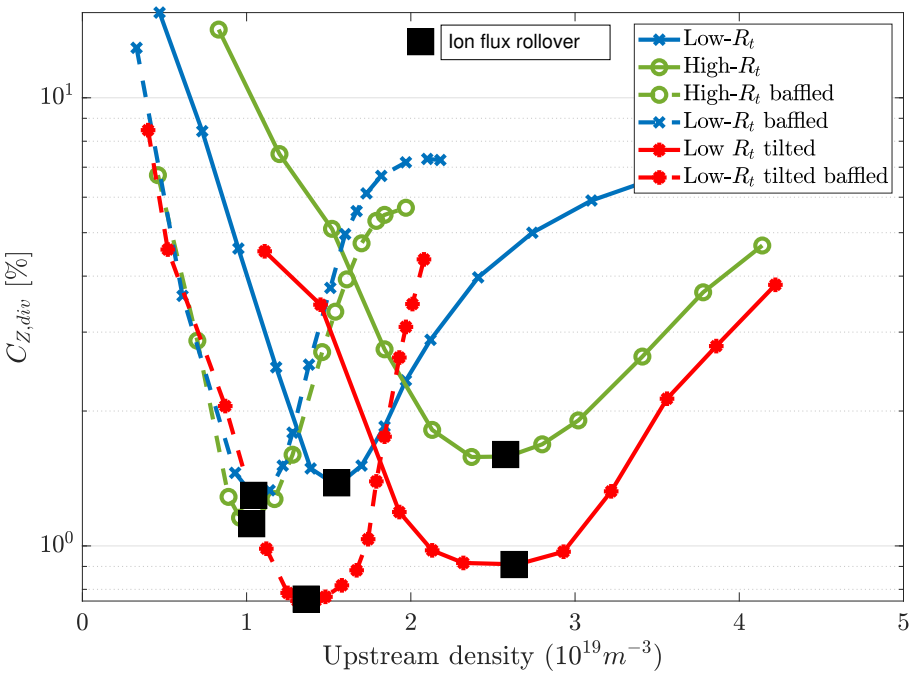

Figure 15: Impurity concentration in the radiating region for all the simulations. The black squares correspond to the simulations at the rollover of the ion flux.

of eq. 4 is a constant and neutral effects were not favoring one configuration over another.

Table 2 shows the values of the relevant variables that we are discussing at the ion flux rollover for all configurations.

Values @ rollover	η_{RI} (%)	n_{eu} (10^{19} m^{-3})	C_Z (%)	$q_{u.\parallel}$ ($MW.m^{-2}$)	$n_{eu}C_Z^{1/2}/q_{u,\parallel}^{5/7}$
Low-R_t	16.8	1.39	1.49	59	0.092
High-R_t	12.3	2.59	1.58	50	0.20
Low-Rt tilted	11.1	2.32	0.92	53	0.13
Low-Rt baffled	18.7	0.93	1.46	65	0.057
High-Rt baffled	17.8	0.96	1.16	64	0.053
Low-Rt tilted baffled	12.3	1.42	0.76	64	0.064

Figure 17 displays the effect of replacing n_{eu} at rollover (used in Fig.14) with $\frac{n_{eu}C_Z^{1/2}}{q_{u,\parallel}^{5/7}}$ at rollover. The differences to Fig. 14 are not very large indicating that variation of n_{eu} is the primary vehicle for reaching detachment. This is shown another way in Fig. 18 where the two axes contain the values at rollover of N_{thres} calculated based only on n_{eu} (x-axis) and based on $\frac{n_{eu}C_Z^{1/2}}{q_{u,\parallel}^{5/7}}$ (y-axis); equation 4 for 3 combinations of

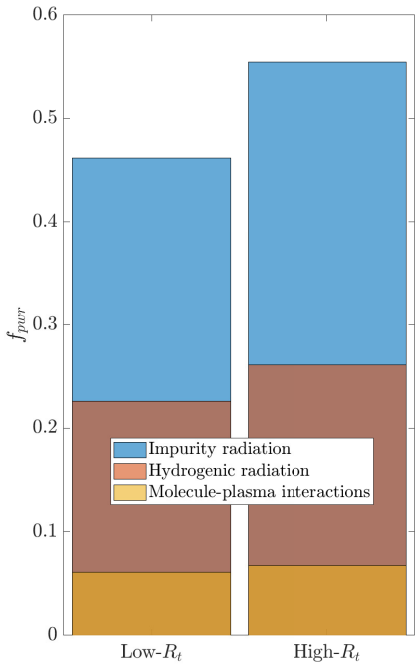

Figure 16: Power balance for the entire outer divertor at rollover, for the low- and high-R_t configurations. About half of the power losses is due to impurity radiation and the rest is divided between hydrogenic radiation and molecule-plasma interactions.

configurations. The predicted value for N_{thres} from the RHS of equation 3 is also shown in Fig. 18 as a red square - a value between 1.18 (if changes in $f(B_t/B_X, l_{div}/L)$ are taken into account) and 1.28 (if changes in $f(B_t/B_X, l_{div}/L)$ are NOT taken into account). The predicted detachment threshold in the three control variables is close to the final configuration comparison - Low-R_t (tilted and baffled) and high-R_t (baffled).

Based on Figure 18 the use of geometry changes to equalize the role of neutrals has roughly recovered the total flux expansion prediction of N_{thres} and thus, at first glance, succeeded. The value of N_{thres} is approximately correct if all control variables are included. However, there is a difference in η_{RI} for the two final cases - Low-R_t (tilted and baffled) and High-R_t (baffled); one would expect that we have equalized η_{RI} between the two. There could, of course, be another variable at play or our definition of η_{RI} is not good enough. Or even more basic, the model embodied in eq. 4 is too simple.

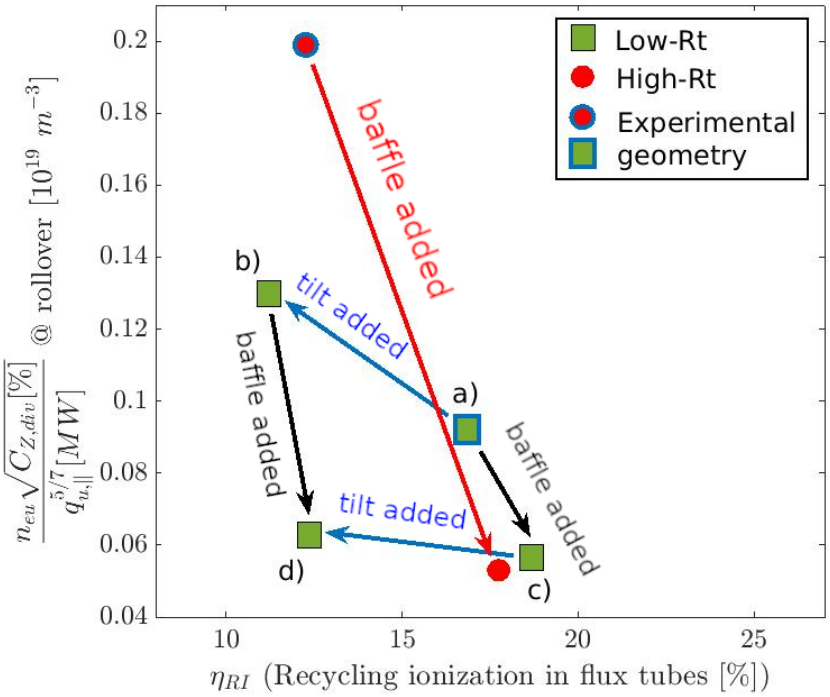

Figure 17: The relationship between $\frac{n_{eu}C_Z^{1/2}}{q_{u,\parallel}^{5/7}}$ at the target ion flux rollover and the percentage of the target ion flux ionizing in the flux tubes studied, η_{RI}.

4.4 Relation to previous work

As mentioned in the Introduction, the effect of total flux expansion was also studied in DIII-D [4]. That excellent study, while not examining the detachment threshold directly, found that within the shelf and floor regions, the temperature and density scaled stronger than R_t^2 as the target major radius was varied within those regions; that is opposite to what we find in the current study and, at first glance, surprising. The DIII-D paper [4] attributes the stronger than scaling observation to "neutral trapping": "*Modelling shows that with greater proximity of the OSP to the baffle structure enhanced neutral trapping occurs. Increased neutral trapping raised recycling, resulting in increased* n_{TAR} *and lowered* T_{TAR}*. This is consistent with observation. As* R_{OSP} *was moved towards the baffle structure, neutral pressure measured in the lower divertor pumping plenum was increased by a factor of 3*". While there is no definition of "neutral trapping" in the paper, it appears that as the strike-point was shifted to larger major radius (R_t or R_{OSP}), effectively a baffle, in the sense of our work was inserted more and more. The central difference to the present work is that for DIII-D, the effective divertor closure improves as R_t is increased, while in TCV, both the divertor closure and the strike-point effect become worse for the high-R_t case. For TCV, this leads to the observed lack of effect of

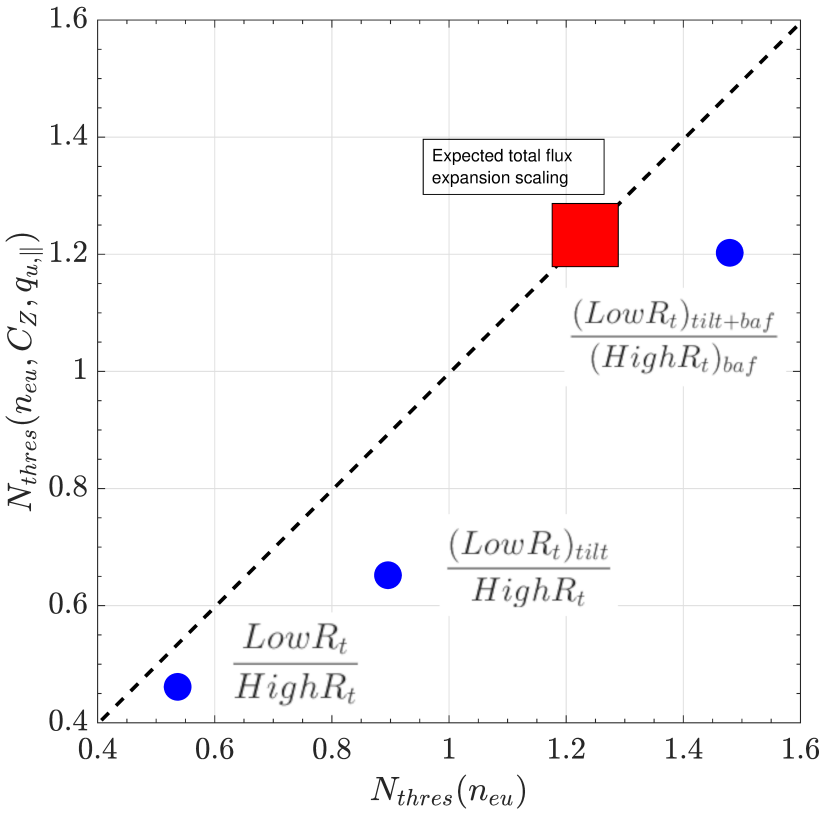

Figure 18: N_{thres} calculated based only on n_{eu} (x-axis) and based on $\frac{n_{eu}C_Z^{1/2}}{q_{u,\|}^{5/7}}$ (y-axis). The red square represents the predicted value for N_{thres} from the RHS of eq.3 (its width represents the error bars of that prediction if we take changes of $f(B_t/B_X, l_{div}/L)$ into account in the calculations or not).

total flux expansion in TCV. Said another way, total flux expansion and divertor closure work together in DIII-D, and against each other in TCV.

While the DIII-D study did not emphasize or separate out the effect of the strike-point angle, other studies have. As pointed out in the introduction, lower strike-point temperatures and lower density detachment thresholds are found for the 'vertical target' [12][15][27][26] than for the 'horizontal target', where the centroid of the recycling neutrals is aimed towards the common flux region. The present results are consistent with the papers cited on this subject.

4.5 Implications for divertor design

The factor of three change in the upstream density detachment threshold found in the variations of magnetic topology and divertor geometry using SOLPS-ITER is a strong argument to include such improvements in any divertor design. In the end, the recipe is fairly straightforward - maximize total flux expansion and

divertor closure, while simultaneously utilizing a separatrix to target angle of the 'vertical target' type (the majority of neutrals headed back towards the separatrix).

The current study is however not exhaustive in exploring the subtleties of arranging the divertor geometry. For example, one could ask if there is a well-defined maximum in neutral trapping as a function of the separatrix to target angle. One could also ask if it matters how small or large the divertor volume is, or how long the divertor legs should be, even though the divertor closure is kept constant.

The results of this study also point towards using modelling to evaluate whether alternative divertor configurations are advantageous for divertor operation or not: Since the effects of magnetic topology are the defining characteristic of alternative configurations, such effects on divertor performance (e.g. detachment threshold, impurity compression, detachment window,...) should be separated out from the effects of divertor geometry (neutrals). Moreover, geometry effects can be used to optimize any divertor topology.

5 Summary

SOLPS-ITER simulations of recent TCV experiments [3] have been able to roughly match the observed lack of effect of total flux expansion predicted by a simple model [8] on lowering the density detachment threshold. Through modelling of variations in the divertor magnetic geometry and magnetic topology, the simulations show that differences in neutral recycling and confinement in the divertor between the low- and high-R_t configurations utilized in the experiment is counteracting the effect of total flux expansion. Removing those differences between low- and high-R_t by forcing both configurations to have identical strike-point angles ('horizontal target') and baffling of the entire outer divertor, we are able to recover the total flux expansion effect. The effect of strike-point angle and overall divertor baffling has been quantified through the introduction of a definition of neutral trapping, η_{RI}. The modification of the divertor geometry through divertor baffling or arranging the strike-point angle to send recycled neutrals towards the separatrix both lower the detachment threshold but lead to different increases in neutral trapping. Those SOLPS-ITER simulations thus confirm the importance of total flux expansion but also show that the neutral trapping properties of the divertor are as important, or more important in TCV, in determining the density detachment threshold. One implication for divertor optimization with respect to lowering the detachment threshold in upstream density, impurity concentration, or increasing the value of P_{SOL} that will allow detachment, is that one should design a divertor with as large a total flux expansion (increase R_t) as possible while simultaneously maximizing the neutral trapping through maximal baffling and utilizing the 'vertical target' strike-point angle.

6 Acknowledgements

This work has been carried out within the framework of the EUROfusion Consortium and has received funding from the Euratom research and training programme 2014-2018 and 2019-2020 under grant agreement No 633053. The views and opinions expressed herein do not necessarily reflect those of the European Commission. This work has also received funding from the EPSRC under the grant EP/N023846/1. The research by B. Lipschultz was funded in part by the Wolfson Foundation and UK Royal Society through a Royal Society Wolfson Research Merit Award as well as by the RCUK Energy Programme (EPSRC grant number EP/I501045). This work was supported in part by the Swiss National Science Foundation. The first author would like to thanks David Moulton for his huge contribution to the SOLPS-ITER post-processing analysis scripts (balance routines, 2PMF equations applied to the SOLPS outputs) which made this work possible. All data created during this research is available in Open access at https://doi.org/10.5281/zenodo.2611209.

References

[1] A. Kallenbach, et al., *Plasma Phys. Control. Fusion* **2013**, *55*, 124441.

[2] M. Wischmeier, et al., *J. Nucl. Mater.* **2015**, *463*, 22-9.

[3] C. Theiler, et al., *Nuclear Fusion* **2017**, *57*, 072008.

[4] T.W. Petrie, et al., *Nuclear Fusion* **2013**, *53*, 113024.

[5] V. A. Soukhanovskii, et al., *Phys. Plasmas* **2012**, *19*, 082504.

[6] V. A. Soukhanovskii, et al., *Journal of Nuclear Materials* **2015**, *463*, 1191-1195.

[7] H. Reimerdes, et al., *Nucl. Fusion* **2017**, *57*, 126007.

[8] B. Lipschultz, et al., *Nuclear Fusion* **2016**, *56*, 056007.

[9] M. Kotschenreuther, et al., *Nuclear Fusion* **2010**, *50*, 035003.

[10] D. Moulton, et al., *Plasma Phys. Control. Fusion* **2017**, *59*, 065011.

[11] M.V. Umansky, et al., *Physics of Plasmas* **2017**, *24*, 056112.

[12] M. Groth, et al., *J. Nucl. Mater.* **2015**, *463*, 471-476.

[13] A. E. Jarvinen, et al., *Plasma Phys. Control. Fusion* **2016**, *58*, 045011.

[14] A. Loarte, et al., *Nuclear Fusion* **1998**, *38*, 331.

[15] B. Lipschultz, et al., *Proc. 16th Int. Conf., IAEA, Vienna* **1996**.

[16] H.-S. Bosch, et al., *Plasma Phys. Control. Fusion* **1999**, *41*, A401-A408.

[17] A. Loarte, et al., *Plasma Phys. Control. Fusion* **2001**, *43*, R183-R224.

[18] D. Ryutov, et al., *Phys. Plasmas* **2007**, *14*, 64502.

[19] B. LaBombard, et al., *Nuclear Fusion* **2015**, *55*, 053020.

[20] M. Kotschenreuther, et al., *Phys. Plasmas* **2007**, *14*, 072502.

[21] P. M. Valanju, et al., *Phys. Plasmas* **2009**, *16*, 056110.

[22] M. Kotschenreuther, et al., *Phys. Plasmas* **2013**, *20*, 102507.

[23] B. Labit, et al., *Nuclear Materials and Energy* **2017**, *12*, 1015-1019.

[24] D. Ryutov, et al., *Phys. Plasmas* **2015**, *22*, 110901.

[25] D. Galassi, et al., *Nuclear Materials and Energy* **2017**, *12*, 953-958.

[26] B. Lipschultz, et al., *Fusion Science and Technology* **2007**, *51:3*, 390-400.

[27] D. Moulton, et al., *Nucl. Fusion* **2018**, *58*, 096029.

[28] W. Morris, et al., *IEEE Trans. Plasma Sci.* **2014**, *42*, 402.

[29] E. Havlíková, et al., *Plasma Phys. Control. Fusion* **2015**, *57*, 15001.

[30] X. Bonnin, et al., *Plasma Fusion Res.* **2016**, *11*, 1403102.

[31] S. Wiesen, et al., *Journal of Nuclear Materials* **2015**, *463*, 480-484.

[32] S. Coda, et al., *Nuclear Fusion* **2017**, *57*, 102011.

[33] J.-M. Moret, et al., *Fusion Eng. Des.* **2015**, *91*, 1.

[34] O. Fevrier, et al., *Rev. of Scient. Instru.* **2018**, *89*, 053502.

[35] K. Verhaegh, et al., *Nuclear Materials and Energy* **2017**, *12*, 1112-1117.

[36] J.R. Harrison, et al., *Plasma Phys. Control. Fusion* **2019**, *61*, 065024.

[37] D. Reiter, et al., *Journal of Nuclear Materials* **1992**, *196*, 80.

[38] R. C. Isler, et al., *Plasma Phys. Control. Fusion* **1994**, *36*, 171.

[39] C. K. Tsui, et al., *Phys. Plasmas* **2017**, *24*, 062508.

[40] A. Fil, et al., *Contributions to Plasma Physics* **2018**, *58*, 746-750.

[41] J.R. Harrison, et al., *Nuclear Materials and Energy* **2017**, *12*, 1071-1076.

[42] P. C. Stangeby, et al., *Nucl. Fusion* **2017**, *57*, 056007.

[43] V. Kotov, et al., *Plasma Physics Control. Fusion* **2009**, *51*, 115002.

[44] M. Wensing, et al., *Plasma Physics Control. Fusion* **2019**, *61*, 085029.

[45] L. L. Lengyel, *Max Planck Institut fur PlasmaPhysik Report IPP* **1981**, *1*, 191.